

Natural orbitals for the *ab initio* no-core configuration interaction approach

Patrick J. Fasano,¹ Chrysovalantis Constantinou,^{1,2,*}

Mark A. Caprio,¹ Pieter Maris,³ and James P. Vary³

¹*Department of Physics and Astronomy,*

University of Notre Dame, Notre Dame, Indiana 46556-5670, USA

²*Center for Theoretical Physics, Sloane Physics Laboratory,*

Yale University, New Haven, Connecticut 06520-8120, USA

³*Department of Physics and Astronomy,*

Iowa State University, Ames, Iowa 50011-3160, USA

(Dated: April 22, 2022)

Ab initio no-core configuration interaction (NCCI) calculations for the nuclear many-body problem have traditionally relied upon an antisymmetrized product (Slater determinant) basis built from harmonic oscillator orbitals. The accuracy of such calculations is limited by the finite dimensions which are computationally feasible for the truncated many-body space. We therefore seek to improve the accuracy obtained for a given basis size by optimizing the choice of single-particle orbitals. Natural orbitals, which diagonalize the one-body density matrix, provide a basis which maximizes the occupation of low-lying orbitals, thus accelerating convergence in a configuration-interaction basis, while also possibly providing physical insight into the single-particle structure of the many-body wave function. We describe the implementation of natural orbitals in the NCCI framework, and examine the nature of the natural orbitals thus obtained, the properties of the resulting many-body wave functions, and the convergence of observables. After taking ${}^3\text{He}$ as an illustrative testbed, we explore aspects of NCCI calculations with natural orbitals for the ground state of the p -shell neutron halo nucleus ${}^6\text{He}$.

* Present address: Computation-Based Science and Technology Research Center, The Cyprus Institute, 2121 Aglantzia, Nicosia, Cyprus

I. INTRODUCTION

The goal of *ab initio* nuclear theory [1–10] is to predict the behavior of the nuclear many-body system starting from underlying internucleon interactions [11–14]. However, the nuclear many-body problem lives in an infinite-dimensional space. Thus, in practical numerical computations, the problem must be replaced by an approximate, truncated representation, and, given finite computational resources, can only be solved with finite accuracy.

This accuracy may be expected to depend critically upon the choice of many-body basis used to define the truncated space for the problem. The many-body basis is in turn generated from some underlying set of single-particle states. More specifically, given the rotational invariance of the nuclear problem, we consider some underlying set of single-particle *orbitals*, of definite angular momentum j . While the choice of orbitals has been a central concern in quantum many-body calculations for the electron structure of atoms and molecules [15], it has been largely neglected in *ab initio* nuclear many-body calculations.

In the no-core configuration interaction (NCCI), or no-core shell model (NCSM), approach [1, 9], the many-body basis consists of antisymmetrized products (Slater determinants) of single-particle states. The many-body problem is then recast as a Hamiltonian matrix eigenproblem in terms of this basis. Harmonic oscillator orbitals [16] have traditionally been used to define the basis for NCCI calculations. This choice is motivated in part by technical convenience. Namely, two-body matrix elements of translationally invariant operators such as the Hamiltonian are conveniently evaluated in the oscillator basis, via the Moshinsky transformation [16] from the relative oscillator basis. Furthermore, an exact separation of the center-of-mass motion is obtained with an oscillator basis truncated according to the N_{max} scheme, *i.e.*, by total number of oscillator excitations [17, 18].

The calculated results for energies, electromagnetic observables, *etc.*, from an *ab initio* NCCI calculation depend on the truncated space in which this calculation is carried out. As N_{max} is increased towards infinity, the calculated results in principle converge towards those which would be obtained in the full, untruncated space for the nuclear many-body problem. However, a rapid growth in dimension of the many-body space, with increasing N_{max} and number of nucleons, limits the accuracy which can be obtained.

Despite the computationally-convenient properties of the harmonic-oscillator orbitals, within a many-body calculation, there is no reason to presume that they are “optimal” as

the underlying single-particle basis for expanding the many-body wave function. Moreover, in at least one way, they are qualitatively mismatched to the problem. Notably, as the solutions to the infinitely-bound harmonic oscillator problem, the oscillator functions fall off at large distance with Gaussian asymptotics, *i.e.*, $\sim e^{-r^2/(2b^2)}$. However, the nuclear attraction is of finite-range. Consequently, the single-particle wave functions arising in mean-field descriptions of the nucleus instead fall off exponentially, *i.e.*, $\sim e^{-\kappa r}$. While a suitable fall-off can be recovered, out to any finite distance of relevance, by taking a superposition of oscillator functions, doing so may require a large number of oscillator functions (see, *e.g.*, Fig. 4 of Ref. [19]).

We are therefore motivated to look beyond the traditional harmonic oscillator many-body basis, to increase the accuracy attainable for a given NCCI problem dimension. In the present work, we explore the improvement which may be obtained by optimizing the choice of underlying orbitals used to construct the basis configurations. While we might simply prescribe a set of orbitals of some analytic form (*e.g.*, Refs. [20, 21]), in the hopes that these might provide some benefit relative to the harmonic oscillator orbitals, a more informed choice can be obtained by first carrying out some preliminary many-body calculation, and using the resulting information on the many-body wave function for guidance in constructing the orbitals.

In this spirit, the *natural orbitals* [22–26] have been used extensively in atomic and molecular electron-structure theory [15, 25], and have also found application in the nuclear problem [27–31]. They are constructed in a way intended to reduce the number of antisymmetrized product states required for an accurate representation of the many-body wave function, thereby accelerating the convergence of its description in a configuration interaction basis [32, 33].

Natural orbitals are defined with reference to some many-body state $|\Psi\rangle$ — not necessarily a single Slater determinant, but a general, correlated many-body state. The corresponding set of natural orbitals is obtained by diagonalizing the one-body density matrix of $|\Psi\rangle$. The eigenvectors define the natural orbitals, and the corresponding eigenvalues represent the mean occupancies of these orbitals within the reference many-body state $|\Psi\rangle$.

In order to find the *true* natural orbitals for a given nuclear state, say, the ground state, we would have to have first solved the full many-body problem for this state, thence obtaining the densities. However, even from an approximate initial solution for the many-body

75 wave function, which yields approximate densities, we may still obtain *approximate* natural
 76 orbitals. It is these which we may attempt to use in constructing an improved basis for the
 77 many-body calculation.

78 Here we explore the use of natural orbitals in NCCI calculations. The initial many-
 79 body calculation, providing the densities used to define the natural orbitals, is a traditional
 80 N_{max} -truncated oscillator-basis calculation. The natural orbitals for a subsequent many-
 81 body calculation are thus obtained as a unitary transformation on the original oscillator
 82 orbitals. In addition to illustrating the convergence properties of the resulting NCCI calcu-
 83 lations, we attempt to illuminate the properties of the natural orbitals and probe some of
 84 the implications for center-of-mass motion.

85 Preliminary results of the present work were reported in Refs. [34, 35]. Complemen-
 86 tary approaches have since also been explored where natural orbitals for use in *ab initio*
 87 nuclear many-body calculations are obtained from solutions of a spatially-localized two-
 88 body (deuteron) problem [36] or from many-body perturbation theory for closed-shell nu-
 89 clei [37, 38]. The implications of natural orbitals for wave function entanglement in NCCI
 90 calculations have also been examined [39].

91 Whereas the preliminary results presented in Refs. [34, 35] were based on the earlier
 92 JISP16 interaction [13], the present examples are based on NCCI calculations using the
 93 Daejeon16 internucleon interaction [40]. Relative to JISP16, Daejeon16 has the advantage
 94 of providing both faster convergence of calculated observables and improved agreement with
 95 experimental binding and excitation energies [41].

96 We first review the framework for calculations with natural orbitals: defining how
 97 symmetry-adapted natural orbitals (of definite angular momentum and parity) are ex-
 98 tracted from the density matrix (Sec. II A) and outlining how these are obtained and used
 99 within the NCCI framework (Sec. II B). Then, to see how the formalism is reflected in
 100 actual NCCI calculations, we take ${}^3\text{He}$ as the simplest nontrivial example: examining the
 101 convergence of energy and radius observables for ${}^3\text{He}$ (Sec. III B), inspecting the radial wave
 102 functions of the natural orbitals themselves (Sec. III B), and diagnosing the center-of-mass
 103 motion of the many-body wave function (Sec. III C). After establishing this baseline, we
 104 explore aspects of NCCI calculations for the neutron halo properties of ${}^6\text{He}$ (Sec. IV).

II. NATURAL ORBITALS

A. Natural orbitals and rotational symmetry

Recall that we seek orbitals which will provide rapid convergence in a finite basis of antisymmetrized product states. Our many-body basis is built out of an ordered set of single-particle orbitals where we favor “lower-lying” orbitals (and disfavor “higher-lying” orbitals) when deciding which orbitals to use in constructing basis states. We would therefore be best served by a set of orbitals such that the “lower-lying” orbitals contribute disproportionately to the most important antisymmetrized products.

It is therefore natural to construct orbitals in a way that maximizes the mean occupation of the lowest-lying orbitals — and, correspondingly, minimizes the mean occupation of the higher-lying orbitals — in the many-body state. In a particle-hole picture, this may be thought of as minimizing the depletion of the Fermi sea. Natural orbitals, in a well-defined sense, accomplish this goal.

Suppose we are interested in finding single-particle states in which to efficiently represent a particular many-body state $|\Psi\rangle$. The single-particle properties of $|\Psi\rangle$ are described by its *one-body density operator* $\hat{\rho}_\Psi$ [42]¹, which is an operator on the single-particle space. *Natural orbitals* are, quite simply, obtained as its eigenstates.

Taken in this traditional sense [22–24], the natural “orbitals” are not orbitals *per se*, as usually construed in nuclear physics. They are, rather, simply a set of independently-defined single-particle states, unrelated to each other by any explicit symmetry constraint. However, one may refine the definition of the natural orbitals, so as to manifestly respect the symmetries of the system [25, 44]. In the case of the rotationally-invariant nuclear problem, the resulting *symmetry-adapted natural orbitals* become orbitals in the usual nuclear-physics sense, of *nlj* orbitals [45]. In the following, we first review the formulation of natural orbitals in the traditional sense, *i.e.*, without explicitly embedding the nuclear symmetries, then establish the symmetry-adapted natural orbitals appropriate to nuclear NCCI calculations.

Although the definition of $\hat{\rho}_\Psi$ as an operator is independent of the choice of basis for the single-particle space, this operator may be expressed in terms of any discrete single-particle

¹ Such a one-body density operator, derived from a pure state of a many-body system, is properly known as a *one-body reduced density operator* [43].

133 basis as

$$\hat{\rho}_\Psi = \sum_{\alpha\beta} |\alpha\rangle \langle\Psi| a_\beta^\dagger a_\alpha |\Psi\rangle \langle\beta|. \quad (1)$$

134 Here, the labels α and β specify the single-particle basis states, *e.g.*, for the nuclear problem,
 135 they may represent the magnetic substates $\alpha = (n_a l_a j_a m_\alpha)$ of nlj orbitals [45], while a_α^\dagger and
 136 a_α represent the creation and annihilation operators, respectively, for a nucleon in state $|\alpha\rangle$.

137 The eigenstates $|\phi_i\rangle$ of $\hat{\rho}_\Psi$ are what we take as the natural orbitals for the many-body
 138 reference state $|\Psi\rangle$. In terms of this eigenbasis, the expression (1) for $\hat{\rho}_\Psi$ reduces to the
 139 familiar canonical form for a density operator as a real linear combination of projection
 140 operators (*e.g.*, Ref. [46]),

$$\hat{\rho}_\Psi = \sum_i \lambda_i |\phi_i\rangle \langle\phi_i|, \quad (2)$$

141 where the λ_i are the corresponding real eigenvalues for the $|\phi_i\rangle$ (we rely here on the obser-
 142 vation that $\hat{\rho}_\Psi$ is a self-adjoint operator).

143 If we work in terms of a discrete basis for the single-particle space, $\hat{\rho}_\Psi$ is represented as
 144 the *one-body density matrix* ρ , with matrix elements $\rho_{\alpha\beta} = \langle\alpha|\hat{\rho}_\Psi|\beta\rangle$, which may be read off
 145 from (1) as

$$\rho_{\alpha\beta} = \langle\Psi| a_\beta^\dagger a_\alpha |\Psi\rangle. \quad (3)$$

146 The operator eigenproblem for $\hat{\rho}_\Psi$ reduces to the matrix eigenproblem for ρ . The eigenvectors
 147 then express the natural orbitals $|\phi_i\rangle$ in terms of the underlying basis. Changing to a natural
 148 orbital basis for the single-particle space makes the density matrix diagonal, with entries λ_i ,
 149 as is apparent from (2).

150 A diagonal matrix element $n_\alpha = \rho_{\alpha\alpha}$ is simply the expectation value of the number
 151 operator $\hat{N}_\alpha = a_\alpha^\dagger a_\alpha$, and thus represents the mean occupation of the single-particle state
 152 α in the many-body state $|\Psi\rangle$. Thus, the eigenvalues λ_i for the natural orbitals $|\phi_i\rangle$ of a
 153 reference state $|\Psi\rangle$ represent their mean occupations in this reference state, *i.e.*, $n_{\phi_i} = \lambda_i$.
 154 Consequently, these eigenvalues must satisfy the properties expected for mean occupations:
 155 $0 \leq \lambda_i \leq 1$ and $\sum_i \lambda_i = A$, where A is the number of nucleons in the system.

156 To see the relevance of the natural orbitals to the problem of identifying an optimal
 157 basis of antisymmetrized product states, first consider the case where $|\Psi\rangle$ is itself a single
 158 antisymmetrized product, specifically, of the first A single-particle states taken from some
 159 particular discrete basis $\{|\alpha_i\rangle\}$, *i.e.*, $|\Psi\rangle = |\alpha_1, \alpha_2, \dots, \alpha_A\rangle$. The one-body density matrix

160 taken in this basis is already diagonal, with occupation numbers $n_{\alpha_i} = 1$ for occupied states
 161 or 0 for unoccupied states [42, 47].

162 If we were instead working in terms of some other single-particle basis $\{|\beta_i\rangle\}$, $|\Psi\rangle$ would
 163 not manifestly be represented as a simple antisymmetrized product state. However, eval-
 164 uating the density matrix in this basis $\{|\beta_i\rangle\}$, and diagonalizing the resulting matrix, will
 165 recover the $\{|\alpha_i\rangle\}$ basis as the natural orbital basis, thereby revealing $|\Psi\rangle$ as a single an-
 166 tisymmetrized product state. (More properly, it will recover the $\{|\alpha_i\rangle\}$ basis to within an
 167 arbitrary freedom of choice of basis within the spaces spanned by the occupied and unoccu-
 168 pied orbitals separately, as each of these represents a degenerate eigenspace of the density
 169 operator, with eigenvalues 1 and 0, respectively.) Such a transformation back to a single
 170 antisymmetrized product state is possible if and only if the density matrix has eigenvalues
 171 which are all either 0 or 1 [43].

172 Of course, we are more generally interested in many-body states which incorporate cor-
 173 relations. There is no single-particle basis in which such a state can be represented as a
 174 single antisymmetrized product, and the eigenvalues of the one-body density operator are
 175 no longer simply 0 and 1.

176 However, the transformation to the natural orbital basis still generates single-particle
 177 states for which the mean occupations “fall as quickly as possible”, in a very particular
 178 sense. Namely, we order the natural orbitals $|\phi_i\rangle$ by decreasing eigenvalue ($\lambda_1 \geq \lambda_2 \geq \dots$),
 179 that is, in order of decreasing mean occupation $n_{\phi_i} = \lambda_i$. The total mean occupation of the
 180 first q single-particle states in any basis is $n_{\leq q} = \sum_{i=1}^q \rho_{ii}$, and the total mean occupation of
 181 the first q natural orbitals, in particular, is $n'_{\leq q} = \sum_{i=1}^q \lambda_i$. By a general property of traces
 182 of Hermitian matrices [48], the partial trace (sum of the first q diagonal entries) in any basis
 183 is bounded from above by the partial trace in the eigenbasis (sum of the first q eigenvalues).
 184 Thus,

$$n_{\leq q} = \sum_{i=1}^q \rho_{ii} \leq \sum_{i=1}^q \lambda_i = n'_{\leq q}. \quad (4)$$

185 That is, for any q , the natural orbitals constitute the basis which maximizes the total mean
 186 occupation of the first q single-particle states [32].

187 The “naive” or generic natural orbitals as defined above, by simply diagonalizing ρ with-
 188 out further precautions, fail to take into account the symmetry properties of the system.
 189 Despite their name, these natural orbitals are simply an independent set of single-particle

states, without well-specified quantum numbers, rather than orbitals *per se*, in the sense that “orbitals” are usually meant in rotationally-invariant problems, as we now elaborate.

Consider, in particular, the symmetries present in nuclear configuration-interaction calculations. To ensure that the many-body space supports states of definite angular momentum and parity, the single-particle states used to build the basis configurations are not arbitrary, but must form orbitals in the traditional shell-model sense. An orbital is a set of magnetic substates $|nljm\rangle$ ($m = -j, \dots, +j$), which together form an angular momentum multiplet of definite j and definite parity $P = (-)^l$. (Since l and j can differ only by $1/2$, the condition of definite parity is sufficient to also enforce definite l .) The different magnetic substates of the orbital are related to each other by angular momentum laddering and share the same radial wave function R_{nlj} .

The many-body reference state $|\Psi_{JM}^P\rangle$ for a nuclear configuration-interaction calculation will have definite angular momentum J , projection M (assuming the problem is formulated in the M scheme [49]), and parity P . These properties of the reference state serve to impose some, but not all, of the requisite properties for the natural orbitals to constitute true nlj orbitals (or the m -substates thereof). By inspection of (3), and the additive nature of the m quantum number, it is clear that the density matrix for a reference state $|\Psi_{JM}^P\rangle$ cannot connect single-particle states $|nljm\rangle$ with different m . Similarly, by the multiplicative nature of parity, it cannot connect single-particle states of different parity.

However, the density matrix will in general connect single-particle states $|nljm\rangle$ with different j , leading to natural orbitals without definite angular momentum.² Due to such considerations, calculations involving natural orbitals are instead commonly based on symmetry-adapted natural orbitals [25, 44]. These are obtained by diagonalizing only that part of the one-body density matrix which is invariant under the action of the symmetry group, namely,

² Only for the special case of a reference state with $J = 0$ do spherical tensor selection rules prevent the density matrix from connecting and thus mixing single-particle states of different j . Even here, caution would be necessary in diagonalizing ρ , as it would contain redundant ljm blocks, one for each $m = -j, \dots, j$. Diagonalizing these blocks together would lead to degeneracies and thus ambiguity (and, in general, undesirable m -mixing) in the choice of eigenstates within each degenerate eigenspace, while diagonalizing each block of definite m independently would still fail to enforce consistent phase relations between the m -substates of an nlj orbital.

for the present problem, angular momentum (and parity).

We construct a rotational scalar one-body density matrix $\bar{\rho}$ in terms of the spherical tensor scalar coupled product [45, 50] of the creation and annihilation operators for an orbital.³ This rotational scalar one-body density matrix has elements

$$\bar{\rho}_{ab} = \langle \Psi_{JM}^P | [a_b^\dagger \tilde{a}_a]_{00} | \Psi_{JM}^P \rangle, \quad (5)$$

or, equivalently, in terms of the original, uncoupled one-body density matrix elements defined in (3), $\bar{\rho}_{ab} = \delta_{j_a j_b} \hat{j}_a^{-1} \sum_m \rho_{(n_a l_a j_a m)(n_b l_b j_b m)}$, where we adopt the notation $\hat{j} \equiv (2j + 1)^{1/2}$.

This scalar density matrix $\bar{\rho}$ is now simply a matrix with respect to orbitals (labeled by a), rather than their magnetic substates (labeled by α). The matrix elements $\bar{\rho}_{ab}$ must be independent of the magnetic substate M of the reference state, since they are given in (5) as the matrix element of a scalar operator in the many-body space.⁴

Nonzero matrix elements $\bar{\rho}_{ab}$ only arise between orbitals of the same angular momentum ($j_a = j_b$), parity, and thus (as argued above) orbital angular momentum ($l_a = l_b$). That is, the scalar one-body density matrix is block diagonal in lj . Symmetry-adapted natural orbitals, obtained as eigenvectors of $\bar{\rho}$, may thus be found by diagonalizing independently within each lj subspace. The resulting natural orbitals are related to the underlying orbitals simply by a unitary transformation

$$|\phi_{n'ljm}\rangle = \sum_n A_{nn'}^{lj} |nljm\rangle \quad (6)$$

on the radial wave functions R_{nlj} within each lj space separately.

The total number operator, summed over all magnetic substates of an orbital, is $\hat{N}_a = \hat{j}_a [a_a^\dagger \tilde{a}_a]_{00}$. Thus, the diagonal matrix elements $\bar{\rho}_{aa}$ of the scalar density matrix are proportional to the mean occupancy of the orbital a ,

$$n_a = \hat{j}_a \bar{\rho}_{aa}, \quad (7)$$

³ The creation and annihilation operators for the magnetic substates $\alpha = (n_a l_a j_a m_\alpha)$ of an orbital $a = (n_a l_a j_a)$ together constitute spherical tensors a_a^\dagger and \tilde{a}_a with components $(a_{n_a l_a j_a}^\dagger)_{m_\alpha} = a_{n_a l_a j_a m_\alpha}^\dagger$ and $(\tilde{a}_{n_a l_a j_a})_{m_\alpha} = (-)^{j_a + m_\alpha} a_{n_a l_a j_a, -m_\alpha}$, respectively [45].

⁴ Alternatively, the vestigial reference to the M quantum number in (5) can be eliminated by recourse to the Wigner-Eckart theorem [50], which gives $\bar{\rho}_{ab} = \hat{j}^{-1} \langle \Psi_J^P | [a_b^\dagger \tilde{a}_a]_0 | \Psi_J^P \rangle$.

which ranges from 0 to the degeneracy $2j_a + 1$ of the orbital. For the symmetry-adapted natural orbital ϕ_a , the corresponding eigenvalue λ_a is then proportional to the mean occupation of the orbital.⁵

Ordering the natural orbitals by decreasing eigenvalue, separately within each lj subspace, serves to define a radial n quantum number, which is now simply a counting index with no strict relation to the number of radial nodes. Ordering by decreasing eigenvalue or, equivalently, decreasing mean occupation, again serves to maximize the occupation of the “lower-lying” orbitals, as in (4), but now only within each lj subspace.

For the rotationally-invariant many-body problem with symmetry-adapted natural orbitals, in contrast to the situation above for “naive” natural orbitals, we would not in general expect the transformation to natural orbitals to reveal a many-body reference state to be a single antisymmetrized product state. Even for a pure shell-model *configuration*, *i.e.*, defined by a specific distribution of nucleons over nlj orbitals, a state of definite J is in general obtained as a linear combination of many such antisymmetrized product states, involving different choices of occupied m -substates for each orbital, as required to couple the angular momenta of the individual nucleons to yield resultant total angular momentum J [49].⁶ Transformation to the symmetry-adapted natural orbitals serves to reveal if a reference state can be represented, not as a single antisymmetrized product state, but rather as a pure shell-model configuration, for some choice of basis orbitals. More generally, it serves to allow the expansion of the many-body wave function in terms of fewer low-lying configurations.

B. Natural orbitals in the NCCI framework

In NCCI calculations [1, 9], the many-body basis consists of antisymmetrized product states built from some underlying orbitals, usually those of the three-dimensional isotropic

⁵ If the spherical tensor annihilation operator in footnote 3 is instead defined with the common alternative phase convention $(\tilde{a}_a)_{j_a, m_a} = (-)^{j_a - m_a} a_{(n_a, l_a, j_a, -m_a)}$ [51], which differs by an overall sign, then we instead have $\hat{N}_a = -\hat{j}_a [a_a^\dagger \tilde{a}_a]_{00}$, and $n_a = -\hat{j}_a \bar{\rho}_{aa}$.

⁶ The notable exception is a closed-shell configuration, for which the resulting $J = 0$ state is indeed simply an antisymmetrized product state.

258 harmonic oscillator. The nuclear Hamiltonian

$$H = T_{\text{intr}} + V + aN_{\text{c.m.}}, \quad (8)$$

259 is then represented as a matrix in terms of this basis. Here T_{intr} is the two-body intrinsic
 260 kinetic energy operator [18, 52, 53], V represents the internucleon interaction (typically
 261 limited to two-body or three-body contributions), and the final Lawson term [49, 54, 55],
 262 proportional to the number operator $N_{\text{c.m.}}$ for center-of-mass oscillator quanta, optionally
 263 serves to control the center-of-mass motion (as discussed further below).

264 The NCCI many-body basis states are defined as antisymmetrized products of single-
 265 particle states described by quantum numbers $nljm$, where n is the radial quantum num-
 266 ber, l the orbital angular momentum, j the resultant angular momentum after coupling to
 267 spin, and m its projection. Each product state thus has definite total angular momentum
 268 projection $M = \sum_{i=1}^A m_i$ and parity $P = \prod_{i=1}^A (-)^{l_i}$. In a typical M -scheme calculation [49],
 269 the basis is restricted to fixed M and P . The individual basis states do not have definite
 270 angular momentum, but, since the Hamiltonian is rotationally invariant,⁷ states of definite
 271 total angular momentum $J \geq |M|$ emerge from the diagonalization.

272 In the usual case where we adopt oscillator orbitals, each orbital is furthermore identified
 273 by its oscillator major shell, or number of oscillator quanta, $N = 2n + l$ [45]. An antisym-
 274 metrized product state then has $N = \sum_{i=1}^A N_i$ oscillator quanta overall, where $N_i = 2n_i + l_i$
 275 represents the number of oscillator quanta contributed by the i th particle. The total number
 276 of quanta may be reexpressed as $N = N_0 + N_{\text{ex}}$, where N_0 is the number of quanta in the
 277 lowest filling of oscillator shells permitted by the Pauli principle for the given nucleus, so
 278 that N_{ex} then represents the number of excitation quanta relative to this lowest filling.

279 The N_{max} truncation scheme restricts the basis configurations to those with $N_{\text{ex}} \leq N_{\text{max}}$,
 280 that is, limiting the total number of excitation quanta. Thus, $N_{\text{max}} = 0$ yields a traditional

⁷ For states of definite total angular momentum to emerge from the diagonalization, the many-body space spanned by this basis should also be “complete” for this purpose, *i.e.*, invariant under rotations. Such is guaranteed in the standard construction procedure for an M -scheme basis, where all m -substates of a given orbital are treated on an equal footing. But this assumption would in general be violated if we were to treat m -substates unequally in the basis truncation, as might happen if we were to work with “naive” natural orbitals (Sec. II A).

“ $0\hbar\omega$ ” shell model space, in which all nucleons are restricted to the valence shell (and an inert core). Since the parity of a harmonic oscillator configuration is $P = (-)^{N_0+N_{\text{ex}}}$, a basis consisting of configurations with $N_{\text{ex}} = 0, 2, \dots, N_{\text{max}}$ (with N_{max} even) yields a truncated space of the same parity as the lowest oscillator configuration (normal parity), while a basis consisting of configurations with $N_{\text{ex}} = 1, 3, \dots, N_{\text{max}}$ (with N_{max} odd) yields a truncated space of the opposite parity (nonnormal parity) [56]. The growth in dimension of the nuclear many-body space with increasing N_{max} is illustrated in Fig. 1, for selected nuclides through the lower *sd* shell.

The truncated space spanned by such a basis, and thus the results of an NCCI calculation, depend on both the many-body basis truncation parameter N_{max} and the oscillator length b of the underlying oscillator single-particle basis. This length scale is commonly quoted as an oscillator energy $\hbar\omega$, in terms of which $b = (\hbar c)/[(m_N c^2)(\hbar\omega)]^{1/2}$, where m_N is the mean nucleon mass ($m_N c^2 \approx 938.92$ MeV). See, *e.g.*, Refs. [57–60] for illustrations of convergence of observables with respect to these basis parameters.

The N_{max} truncation for the oscillator basis holds a special place in NCCI calculations due to its properties regarding center-of-mass motion. The physically-relevant degrees of freedom for describing nuclear structure and excitations reside in the motion of the nucleons relative to their common center of mass, rather than in the motion of this center of mass relative to the laboratory frame. However, given that the NCCI approach is formulated in terms of antisymmetrized products of single-particle states defined with respect to the laboratory frame, the center-of-mass coordinate cannot be strictly eliminated as a degree of freedom in the many-body wave function. Nonetheless, this motion can at least be brought into a known, controlled form.

Namely, the N_{max} truncation, in particular, ensures that nuclear eigenstates can be obtained exhibiting an exact separation between a pure oscillator $0s$ wave function for the center of mass coordinate (*i.e.*, the center-of-mass degree of freedom is frozen into its zero point motion) and an intrinsic wave function for the motion of the nucleons relative to each other (see Sec. II B of Ref. [18] for a detailed explanation of the reasoning). The Lawson term in (8) selects such eigenstates with $0s$ center-of-mass motion, by shifting any remaining states involving center-of-mass excitation out of the low-lying spectrum. Thus, states involving excitation of the intrinsic wave function are cleanly separated from what would otherwise be a thicket of spurious excitations in the calculated spectrum (see Fig. 8 of Ref. [20] for an

illustration of the effect on the spectrum). Moreover, such factorization greatly simplifies the calculation of certain observables, including the r.m.s. radius, electric monopole ($E0$), magnetic dipole ($M1$), and electric quadrupole ($E2$) observables [18].

Here it is important to note that the factorized $0s$ center-of-mass wave function thus obtained has an oscillator parameter $\hbar\omega_{\text{c.m.}} = \hbar\omega$ which is determined by the oscillator parameter of the underlying single-particle basis. Equivalently, in terms of oscillator lengths, the $0s$ wave function in the center-of-mass coordinate has an $\hbar\omega$ -dependent oscillator length $b_{\text{c.m.}} = A^{-1/2}b$ (see Sec. F.3 of Ref. [18]). Thus, many-body calculations carried out in N_{max} -truncated oscillator bases of different $\hbar\omega$ result in different “spectator” center-of-mass motions. That is, the many-body eigenstates obtained using these different bases may converge towards the same intrinsic structure with increasing N_{max} , but not the same center-of-mass wave function. This will be important to keep in mind when interpreting the $\hbar\omega$ -dependence of the natural orbitals thus obtained (as in Sec. III B below).

If we move beyond the traditional oscillator basis in N_{max} truncation, as we must to make use of natural orbitals, we forsake the formal comfort of having a guaranteed exact center-of-mass factorization. However, in practice, an approximate factorization may still be obtained [20, 61–63], either since it naturally emerges in the calculation (as explored for the natural orbital basis in Sec. III C below) or with some help from a Lawson term. Furthermore, the impact upon observables of any spurious contribution may be mitigated through judicious use of translationally-invariant intrinsic operators [18].

Indeed, alternate choices both for orbitals and for truncation have already been applied in NCCI calculations. For instance, orbitals defined in terms of the Laguerre functions [64–66], a standard set of basis functions in electron-structure theory [15], have been explored [20, 21].

For the many-body truncation, calculations have also been performed using the so-called full configuration interaction (FCI) truncation [15], which simply retains all configurations built by distributing nucleons over the given set of orbitals (this is simply the traditional fermionic many-body space obtained from a given set of single-particle states [67]). In the context of NCCI calculations, the FCI basis is taken as all configurations involving a given set of oscillator shells. However, convergence with respect to the many-body basis size is found to be much slower than for traditional N_{max} calculations [68]. More general many-body truncation schemes⁸ are also feasible, *e.g.*, in which orbitals are weighted by measures

⁸ Here we specifically have in mind truncation schemes for a traditional configuration interaction basis of

other than the number of oscillator quanta [70] or in which the basis configurations are selected through more sophisticated importance criteria [71].

Regardless of basis choice, the essential inputs into the construction of the Hamiltonian matrix in the NCCI basis are the two-body matrix elements of this Hamiltonian (assuming the internucleon interaction V is two-body, or three-body matrix elements, if the interaction is three-body, *etc.*). These must be obtained for the given choice of orbitals. The rest of the Hamiltonian construction follows from the standard treatment of n -body operators in second quantization [67]. The eigenproblem is thus cast as a large, sparse matrix diagonalization problem, which is solved numerically using, *e.g.*, the Lanczos algorithm [49, 72].

One-body densities are readily extracted from the resulting wave functions. These densities are commonly used for the computation of one-body observables, such as matrix elements of electromagnetic operators for moments and transitions [45], and as inputs to reaction calculations [73]. More precisely, while the electromagnetic operators, taken properly in the center-of-mass frame, involve two-body or higher contributions, they may effectively be replaced by one-body operators when the center-of-mass motion has the harmonic-oscillator 0s form noted above [18, 74]. The scalar densities (5), in particular, are also the necessary ingredient for deducing natural orbitals appropriate to the NCCI framework (Sec. II A).

Our procedure is thus to carry out an initial NCCI calculation in a traditional N_{\max} truncated oscillator basis. One of the calculated eigenstates, say, the ground state, is taken as the reference state for generating natural orbitals, and the relevant scalar densities are extracted.

To see which oscillator orbitals contribute to the resulting natural orbitals, note that, in an N_{\max} -truncated NCCI basis, the configurations involve nucleons reaching orbitals with N_{\max} quanta above the valence shell. The active orbitals thus have $N \leq N_v + N_{\max}$, where N_v is the number of oscillator quanta for the valence shell (*e.g.*, $N_v = 0$ for an “ s -shell” nucleus, or $N_v = 1$ for a “ p -shell” nucleus). The calculated scalar densities reflect only these active orbitals, and the natural orbitals resulting from diagonalizing the resulting density

antisymmetrized product states. It should be noted that symmetry-adapted coupling schemes for NCCI calculations, based on $SU(3)$ [8] or $Sp(3, \mathbb{R})$ [69] symmetry groups, are subject to truncation schemes of a different nature, as these schemes involve a change of basis, before truncation, to correlated many-body basis states.

matrix represent mixtures of only these orbitals, that is, oscillator orbitals of the same (lj) and with $N \leq N_v + N_{\max}$.

The resulting natural orbitals are again labeled by quantum numbers nlj , where now the radial quantum number n no longer necessarily reflects the number of nodes in the radial wave function but simply reflects the chosen ordering of natural orbitals by decreasing eigenvalue (*i.e.*, decreasing mean occupancy) as discussed above (Sec. II A). For example, consider an $N_{\max} = 4$ calculation for the s -shell nucleus ${}^4\text{He}$. Within the $s_{1/2}$, or $(l, j) = (0, 1/2)$, subspace, the resulting scalar densities connect the $0s_{1/2}$, $1s_{1/2}$, and $2s_{1/2}$ orbitals ($N = 0, 2, 4$, respectively), and diagonalizing the scalar density matrix thus mixes these orbitals to define natural orbitals $0s'_{1/2}$, $1s'_{1/2}$, and $2s'_{1/2}$.

It is now straightforward to carry out an NCCI calculation in a new basis, formed from antisymmetrized products of natural orbitals. The same many-body machinery is used as in the original oscillator-basis calculation. It is merely necessary to carry out a change of basis [75] on the two-body matrix elements of the Hamiltonian (8) (see Sec. III C of Ref. [20]). Only a finite set of two-body matrix elements in the oscillator basis are required as input to the transformation, since, as just noted, each natural orbital is obtained from a finite set of underlying oscillator orbitals. Then, evaluation and diagonalization of the many-body Hamiltonian matrix proceed as before.

However, in defining an NCCI calculation in terms of natural orbitals, a fundamental question arises as to how to truncate the many-body basis. The choice may be expected to profoundly affect the results and, in particular, determine how the accuracy obtained from the many-body calculation relates to basis size.⁹

The transformation from oscillator orbitals to natural orbitals is simply a unitary transformation on the single-particle space. More specifically, this transformation is restricted to the low-lying subspace spanned by oscillator states with $N \leq N_v + N_{\max}$. Since the many-body basis consists of antisymmetrized products of the single-particle orbitals, a change of basis on the single-particle space inherently induces a change of basis on the many-body product space.

However, if all antisymmetrized products are retained, as in the FCI truncation, then,

⁹ Admittedly, this same comment applies to the choice of truncation scheme for NCCI calculations defined in terms of oscillator orbitals as well, discussed above, where the freedom of choice is commonly ignored.

while the basis itself may change, the many-body space spanned by this basis is invariant under such a rearrangement of the single-particle space. Thus, an FCI calculation based on the original oscillator orbitals, or on natural orbitals obtained by a unitary transformation of these, yield identical results. No benefit in convergence is achieved. The truncated many-body spaces obtained before and after transformation to natural orbitals only differ when the set of antisymmetrized product states constituting the many-body basis is truncated in a nontrivial fashion, that is, to a proper subspace of the FCI space (as compared in Sec. III A below). The dimension of the N_{\max} truncated space and the enveloping FCI space involving the same orbitals (dotted line) for ${}^3\text{He}$ may be compared in Fig. 1.

An obvious, though not necessarily optimal, choice of many-body truncation scheme, as adopted here, is to simply carry over the formal structure of the N_{\max} truncation. The natural orbitals are already identified by nlj labels, where, again, n reflects the chosen ordering by decreasing occupancy in the reference state. For each of these orbitals, we may simply define a weighting label $N = 2n + l$ (as in Refs. [20, 37]), although this label no longer has any direct meaning in terms of oscillator quanta. We then proceed as before, by treating this label as an additive quantity, thereby defining $N = \sum_{i=1}^A N_i$ for a many-body configuration, and imposing a nominal N_{\max} truncation on the configurations. This truncation no longer has any direct connection to the oscillator excitation quanta in the system, nor does it guarantee exact center-of-mass separability. However, conveniently for purposes of comparison, the dimension of the problem is exactly as it was for the original N_{\max} -truncated oscillator basis (Fig. 1).

III. ILLUSTRATION OF NATURAL ORBITALS IN NCCI CALCULATIONS:

${}^3\text{He}$

A. Convergence of observables

To see how the formalism just elaborated (Sec. II) is reflected in actual NCCI calculations, let us now examine the convergence of observables in illustrative NCCI calculations, making use of symmetry-adapted natural orbitals. Here we take ${}^3\text{He}$ as the simplest nontrivial example. The comparatively slow growth of dimension with N_{\max} for this nuclide (Fig. 1) means that essentially converged results can be obtained, as a reference against which the

convergence of lower- N_{\max} results can be compared.

Results for the ground state energy eigenvalue of ${}^3\text{He}$ are shown in Fig. 2, first as obtained in the oscillator basis [Fig. 2(a)], then as obtained in the natural orbital basis [Fig. 2(b)]. For these illustrations, we take the Daejeon16 internucleon interaction [40], which is based on the two-body part of the Entem-Machleidt (EM) N^3LO chiral EFT interaction [12], subsequently softened via a similarity renormalization group (SRG) transformation [76] to enhance convergence and then adjusted via a phase-shift equivalent transformation to provide better description of nuclei with $A \leq 16$. Calculations are obtained using the many-body code MFDn [77, 78], along with codes for the transformation of two-body matrix elements from the oscillator basis to the natural-orbital basis [79], and no Lawson term [see (8)] is included in the Hamiltonian for the calculations in the natural-orbital basis. We also show the experimental binding energy [80] for comparison.

The eigenvalues obtained in the oscillator-basis calculations [Fig. 2(a)] follow a familiar convergence pattern (*e.g.*, Refs. [58, 76]). Each curve represents calculations at fixed N_{\max} (from 8 to 16), for varying $\hbar\omega$, and has a variational minimum with respect to $\hbar\omega$, which arises in the vicinity of $\hbar\omega = 12.5\text{ MeV}$ for this particular nuclide, state, and interaction. Increasing N_{\max} , at given $\hbar\omega$, strictly expands the space in which the calculation is carried out, and is thus guaranteed by the variational principle to monotonically lower the ground state energy. Convergence towards the true eigenvalue, as would be obtained in the full, untruncated many-body space, is signalled by insensitivity to the basis truncation N_{\max} (compression of successive curves), as well as local insensitivity to the oscillator parameter $\hbar\omega$ (flattening of the curves). For the ground state energy, this manifests as compression of the curves against a variational floor.

For each of these oscillator-basis calculations, the resulting one-body densities yield a set of approximate natural orbitals, which define the natural orbital basis, which we then use for a subsequent many-body calculation, as outlined in Sec. II B. For the resulting energies [Fig. 2(b)], each curve again represents calculations at fixed N_{\max} , now in the sense of the nominal N_{\max} truncation scheme for natural orbitals (Sec. II B).

Comparing the overall shapes of the curves, of E *vs.* $\hbar\omega$, in Fig. 2, we may observe that the natural-orbital basis provides an overall flattening, or reduced dependence on $\hbar\omega$, in the vicinity of the variational minimum. However, for a more direct quantitative comparison of the results obtained with the two bases, the approximately exponential nature of the

convergence with N_{\max} [76, 81, 82] means that comparison can be carried out more readily on a logarithmic scale. To provide a meaningful zero point for the logarithmic scale, we must take the residual with respect to a “converged” reference value E_{ref} , which we obtain from higher- N_{\max} calculations (for $N_{\max} \approx 24$, the energy in the vicinity of the variational minimum is converged to the keV scale). The energies, thus recast as residuals, are shown on a logarithmic scale in Fig. 2(c), for the results obtained both with the oscillator (filled circles) and natural-orbital (open squares) bases. To provide clear separation in the plot, only the $N_{\max} = 8, 14$, and 16 results are shown.

At lower N_{\max} , as exemplified by the $N_{\max} = 8$ results (dotted lines) in Fig. 2(c), there is little distinction between the results obtained in oscillator and natural-orbital bases. This is perhaps to be expected. In the limit of $N_{\max} = 0$, the bases for the oscillator and subsequent natural-orbital calculations are strictly identical. More generally, a low- N_{\max} underlying oscillator calculation provides little opportunity for high- N orbitals to appear in the densities and thus natural orbitals.

At higher N_{\max} , as exemplified by the $N_{\max} = 14$ and 16 results (dashed and solid lines, respectively) in Fig. 2(c), one way of comparing the results is to measure the advance obtained by the transformation to natural orbitals in terms of the equivalent increase in N_{\max} required with a traditional oscillator basis to achieve the same advance. In this sense, for calculations in the vicinity of the variational minimum, the energies obtained with natural orbitals are approximately “one step” in N_{\max} ahead of those obtained with oscillator orbitals. Away from the variational minimum, the advantage provided by the natural orbitals is more marked, reflecting the comparative $\hbar\omega$ -independence already noted for these calculation in the natural-orbital basis.

Alternatively, we may assess the results of the change of basis in terms of the fraction by which it reduces the residual, *i.e.*, how far it brings us towards the true value which would be obtained in the full, untruncated space. On a logarithmic scale, a given downward vertical shift represents a given fractional reduction. Comparing the $N_{\max} = 16$ results obtained in the two bases, we may observe an approximately uniform downward shift, across the range of $\hbar\omega$, representing a reduction in the residual by a factor of ~ 3 (a somewhat greater reduction is attained with the natural-orbital basis for $\hbar\omega \approx 10$ MeV).

However, there is an obvious bound on the improvement which may be expected from the transformation to the natural-orbital basis derived from an N_{\max} -truncated oscillator

493 basis calculation. Recall that the active orbitals in the oscillator-basis calculation and the
 494 subsequent natural orbitals span the same single-particle space. Both the N_{max} -truncated
 495 oscillator basis and the nominally N_{max} -truncated constructed from the ensuing natural
 496 orbitals span subspaces of the same enveloping FCI space defined by those orbitals (Sec. II B).
 497 This FCI space is, in general, of much higher dimension [68]. *E.g.*, for an $N_{\text{max}} = 10$
 498 calculation for ^3He , which has dimension 2.6×10^4 , the FCI space consists of all product
 499 states involving orbitals through the $N = 10$ oscillator shell, which has the substantially
 500 larger dimension 2.8×10^6 (Fig. 1). We might hope that the N_{max} -truncated natural orbital
 501 basis might allow us to reach comparable accuracy in a much smaller space, but it cannot
 502 access any components of the true wave function which lie outside of the FCI truncated
 503 space.

504 For the ground state energy, in particular, the result in the FCI space provides a varia-
 505 tional lower bound on the results in the subspaces. Thus, it is informative to compare the
 506 improvement obtained with natural orbitals to the maximum improvement which could be
 507 obtained in the enveloping FCI space. The calculated ^3He ground state energies obtained
 508 in the oscillator basis (filled circles) and natural-orbital basis (open squares) are compared
 509 with the variational bound provided by the enveloping FCI space (filled triangles) in Fig. 3.
 510 Here again, as in Fig. 2(c), values are shown as residuals relative to the true energy, on a
 511 logarithmic scale.

512 At low N_{max} , as exemplified by the $N_{\text{max}} = 4$ results (dotted lines), a factor of ~ 3
 513 improvement is possible within the FCI space, near the variational minimum and over most
 514 of the $\hbar\omega$ range shown. Yet, as already noted, the transformation to natural orbitals conveys
 515 negligible benefit, at least within the nominal N_{max} truncation scheme.

516 At higher N_{max} , as exemplified by the $N_{\text{max}} = 10$ results (solid lines), the improvement
 517 possible within the FCI space ranges from a factor of ~ 4 , at the extreme $\hbar\omega$ shown,
 518 to an order of magnitude, near the variational minimum. Near the variational minimum,
 519 the improvement attained in the natural-orbital basis, which reduces the residual by less
 520 than a factor of 2, is by this measure perhaps disappointing. Further from the variational
 521 minimum, however, the improvement afforded by the N_{max} -truncated natural-orbital basis
 522 becomes an appreciable fraction of that possible within the FCI space. A natural question
 523 is whether the improvement possible within the FCI space could be more fully achieved,
 524 still with a reduction in dimension comparable to that afforded by the N_{max} truncation

scheme, but under a more physically-informed truncation scheme, *e.g.*, one which makes use of the information on expected occupancies of the orbitals provided by the eigenvalues of the density matrix.

As an initial illustrative example of the convergence obtained for an observable other than the energy, we consider the point-proton root-mean-square (r.m.s.) radius r_p of the ^3He ground state. (The point-proton radius is simply related to the physically-accessible charge radius r_c [83], after hadronic physics corrections [84, 85].) The r.m.s. radius, like electric quadrupole ($E2$) observables, is sensitive to the large-radius behavior of the wave function, as the r^2 operator more heavily weights the tails of the wave functions. The convergence of such observables is therefore notably troublesome in NCCI calculations in an oscillator basis [57, 58, 60]. However, improved asymptotic behavior of the single-particle basis, as one anticipates with the natural orbitals (and as illustrated below in Sec. IIIB), might therefore be expected to particularly impact the convergence of such observables.

The calculated results for r_p are shown in Fig. 4, where the values obtained with the oscillator (filled circles) and natural-orbital (open squares) bases are overlaid. An approach to convergence is signaled by the “shouldering” of the curves, to form a region of local $\hbar\omega$ -independence (flattening) and compression of curves for successive N_{max} against each other. The value for r_p deduced from the experimental r_c [83] is shown for comparison (filled diamond).

The oscillator-basis calculations for the radius are already atypically well-converged for ^3He (compare, *e.g.*, Sec. IV below). Note the highly expanded vertical scale in Fig. 4 (on the scale of 0.1 fm overall). For the underlying oscillator calculations (filled circles), the various curves for different N_{max} (from 10 to 16) cross in the vicinity of $\hbar\omega = 10$ MeV. (Such crossings have been suggested, purely heuristically, as a means of estimating the true radius as it would be obtained in the full, untruncated space [57, 86, 87], though in practice this prescription must be treated with caution [21].)

The subsequent calculations in the natural-orbital basis (open squares) do not share such a sharply-defined crossing point. Rather, they more clearly demonstrate the traditional hallmarks of convergence, namely, flattening and compression of the curves. For instance, the $N_{\text{max}} = 16$ curve varies by $\lesssim 0.04$ fm over the range of $\hbar\omega$ from 10 MeV to 20 MeV, while the $N_{\text{max}} = 14$ and 16 curves differ by less than $\lesssim 0.01$ fm over this same range. As a consequence of this flattening, by the high end of the $\hbar\omega$ range shown ($\hbar\omega = 25$ MeV), the calculations

in the natural-orbital basis lie two steps in N_{\max} “ahead” of the calculation in the oscillator basis. The question, of course, is how this difference in convergence behavior actually aids in the problem of direct interest in less well-converged cases, which is to accurately estimate the true value of the observable, as it would be found in the full, untruncated space.

B. Natural orbitals

Let us now examine the natural orbitals obtained (and subsequently used) in the present ${}^3\text{He}$ calculations, with the aim of understanding their dependence on the underlying oscillator calculation and thereby also of gaining some insight into their influence on the convergence of observables in the many-body calculation. Recall that the natural orbitals in these many-body calculations are approximations to the “true” natural orbitals for the ${}^3\text{He}$ ground state, since they are deduced from the approximate ${}^3\text{He}$ ground state densities obtained in finite, truncated oscillator-basis NCCI calculations (Sec. II B). The densities, and thus the resulting natural orbitals, depend upon both the N_{\max} and $\hbar\omega$ of the underlying oscillator-basis calculation.

Recall, furthermore, that the symmetry-adapted natural orbitals (Sec. II A) appropriate to NCCI calculations preserve the l and j quantum numbers, changing only the radial wave function, by “mixing” underlying oscillator orbitals of different n within an lj space. We focus first on the $0s_{1/2}$ orbital, as this is the notionally “occupied” orbital in a simple shell-model picture, and is indeed still the most heavily-occupied orbital in the actual NCCI calculations. We then explore the properties of the notionally “unoccupied” excited orbitals. While the occupations of these excited (or notionally unoccupied) orbitals are comparatively small, it is these orbitals which drive the convergence of the many-body calculation in a natural-orbital basis.

The radial wave function for the $0s_{1/2}$ natural orbital for protons, in particular, is shown in Fig. 5, where its dependence on the N_{\max} and $\hbar\omega$ of the underlying oscillator calculation is mapped out. (The behavior for the neutron $0s_{1/2}$ orbital is qualitatively similar.) Here, the radial wave function is plotted as the radial probability density $P(r) = r^2|\psi(r)|^2$, from $N_{\max} = 2$ (dotted lines) to $N_{\max} = 16$ (solid lines), separately for $\hbar\omega = 9$ MeV [Fig. 5(a)], 15 MeV [Fig. 5(b)], and 25 MeV [Fig. 5(c)]. The $0s$ radial function for the underlying oscillator basis is also shown for comparison (thick gray line). Note that the natural orbital

587 obtained from an $N_{\text{max}} = 0$ oscillator calculation is still simply this oscillator function, as the
 588 resulting densities do not mix the fully-occupied s -shell orbitals with the fully-unoccupied
 589 higher orbitals.

590 The densities, and thus the resulting natural orbitals, are expected to eventually converge
 591 with increasing N_{max} . Such is indeed seen in Fig. 5, if we examine the curves within a given
 592 panel, *i.e.*, obtained for different N_{max} but at a given choice of $\hbar\omega$. On this scale, the shape
 593 of the radial wave function appears to change comparatively little for N_{max} beyond about 4
 594 or 6.

595 The $\hbar\omega$ dependence is more subtle. All observables (energies, electromagnetic matrix
 596 elements, radii, *etc.*) obtained from the densities retain some $\hbar\omega$ dependence at finite N_{max}
 597 due to their sensitivity to the N_{max} - and $\hbar\omega$ -dependent *intrinsic* structure of the approximate
 598 ${}^3\text{He}$ ground state obtained in a truncated oscillator calculation. At finite N_{max} , some $\hbar\omega$
 599 dependence of the natural orbitals may similarly be expected to arise from such sensitivity
 600 to the N_{max} - and $\hbar\omega$ -dependence of the calculated intrinsic structure. This dependence is
 601 expected to ultimately disappear with increasing N_{max} , as the intrinsic structure converges.

602 However, recall (Sec. II B) that even in the large N_{max} limit the natural orbitals for the
 603 NCCI problem are not uniquely defined. Rather, they may be expected to have an inherent
 604 $\hbar\omega$ -dependence arising from the *center-of-mass* zero-point motion of the reference many-
 605 body state, which varies with the $\hbar\omega$ of the underlying oscillator basis. Thus, it should
 606 not be surprising that, even at high N_{max} , the natural orbitals obtained from underlying
 607 oscillator-basis calculations with different $\hbar\omega$ do not coincide. Compare the solid curves
 608 in the different panels of Fig. 5. These clearly do not coincide, with the location of the
 609 maximum moving to smaller radius with increasing $\hbar\omega$.

610 To characterize how the radial wave functions for the natural orbitals at high N_{max} (solid
 611 lines) differ qualitatively from those of the underlying oscillator functions (thick gray lines),
 612 in Fig. 5, we shall find it convenient to separately consider the central region of the wave
 613 function and its large-radius tail (porous though this distinction may be). Let us first
 614 consider the central region, that is, around the peak in the wave function.

615 For the $0s_{1/2}$ natural orbital obtained from the reference wave function calculated in
 616 an $\hbar\omega = 15\text{ MeV}$ oscillator basis [Fig. 5(b)], there is little apparent change going from
 617 the underlying oscillator function to the natural orbital. For the natural orbital obtained
 618 in an $\hbar\omega = 9\text{ MeV}$ oscillator basis [Fig. 5(a)], which has a longer oscillator length [recall

619 $b \propto (\hbar\omega)^{-1/2}$], the peak shifts inward, to lower radius, relative to the underlying oscillator
 620 function, though not all the way to the peak location for $\hbar\omega = 15$ MeV [Fig. 5(b)]. Al-
 621 ternatively, for the natural orbital obtained in an $\hbar\omega = 25$ MeV oscillator basis, which has
 622 a shorter oscillator length [Fig. 5(c)], the peak shifts outward, to larger radius, relative to
 623 the underlying oscillator function, though again not all the way to the peak location for
 624 $\hbar\omega = 15$ MeV.

625 Either way, a portion of the effect of transforming from the underlying oscillator basis
 626 to natural orbitals is to “dilate” the radial function to more closely resemble a $0s$ oscillator
 627 function of $\hbar\omega \approx 15$ MeV. The effect is to moderate the change in characteristic length scale
 628 for the natural orbitals, as the $\hbar\omega$ for the underlying oscillator basis is varied, as compared
 629 to the change in oscillator length for the underlying oscillator orbitals themselves. This
 630 reduced $\hbar\omega$ dependence of the orbitals (at least in the central region) presumably contributes
 631 to the reduction in $\hbar\omega$ dependence found for the observables in the calculations based on
 632 the natural-orbital basis (Sec. III A).

633 A simple and intuitive explanation for this behavior of the orbitals is that the natural
 634 orbitals are the result of a compromise between the intrinsic structure and center-of-mass
 635 motion embodied within the reference wave function. The intrinsic structure is described well
 636 by nucleons occupying orbitals resembling an $\hbar\omega = 15$ MeV $0s_{1/2}$ oscillator orbital, regardless
 637 of underlying oscillator basis. But the center-of-mass motion of the reference wave function
 638 for $\hbar\omega = 9$ MeV is well described by nucleons in an $\hbar\omega = 9$ MeV $0s_{1/2}$ oscillator orbital.
 639 The resulting $0s_{1/2}$ natural orbital lies somewhere inbetween. Similarly, the center-of-mass
 640 motion of the reference wave function for $\hbar\omega = 25$ MeV is well described by nucleons in an
 641 $\hbar\omega = 25$ MeV $0s_{1/2}$ oscillator orbital, and the resulting $0s_{1/2}$ natural orbital lies somewhere
 642 inbetween.

643 Turning now to the tail region of the orbital, the natural question is the extent to which
 644 the natural orbitals take on the exponential asymptotics anticipated from the mean-field
 645 description of the nucleus. Recall that these asymptotics are expected to be particularly
 646 important for the convergence of long-distance observables (Sec. III A).

647 The asymptotic behavior is more readily apparent if we replot the radial probability
 648 densities on a logarithmic scale, as in Fig. 6. A tail with exponential asymptotics appears
 649 as a straight line on such a plot, while a tail with the Gaussian asymptotics characteristic of
 650 the oscillator functions appears as downward-curving parabola, as seen for the underlying

oscillator radial functions (grey lines). We may observe that the tail “grows in”, with the inclusion of additional oscillator functions, so that exponential asymptotics (*i.e.*, straight-line falloff on the log plot) are gradually established, extending to larger radii with increasing N_{\max} . (One may compare to Fig. 4 of Ref. [19], for a classic illustration of an exponential tail growing in for a Hartree-Fock orbital, or to Fig. 1 of Ref. [21], for the schematic example of a Woods-Saxon orbital expanded in an oscillator basis [45].) The emergence of exponential asymptotics is most clearly visible for the $\hbar\omega = 15$ MeV natural orbitals [Fig. 6(b)], where the progression from the underlying oscillator orbital to the true, high- N_{\max} natural orbital is not complicated by a significant radial shift in the peak location.

NCCI calculations for ^3He in a natural-orbital basis involve, of course, not just the notionally occupied $0s_{1/2}$ orbital, but also basis configurations incorporating the higher, notionally unoccupied, natural orbitals, as well. Some of the low-lying natural orbitals are shown in Fig. 7, for both protons (short dashed lines) and neutrons (long dashed lines). Here we follow the analogy to an oscillator basis, by focusing on natural orbitals with nlj quantum numbers corresponding to the traditional $N = 0$ (s), 1 (p), and 2 (sd) oscillator shells. We focus on the natural orbitals obtained from the $\hbar\omega = 15$ MeV oscillator-basis calculation at $N_{\max} = 16$, so that the proton $0s_{1/2}$ orbital here corresponds to the highest- N_{\max} case shown in Fig. 5(b). Again, the underlying oscillator orbital is shown for comparison (thick gray lines).

Let us first consider the “occupations” (7) of these orbitals in the reference wave function, which we know from the corresponding eigenvalues of the scalar density matrix (Sec. II A). (Such occupations provide only an estimate of the occupation in any subsequent many-body calculation using the natural-orbital basis.) The occupations are shown graphically at the top of each panel in Fig. 7, but at this scale are indistinguishable from those of the traditional shell model description (in which $n_{0s_{1/2}} = 1$ for the neutrons, $n_{0s_{1/2}} = 2$ for the protons, and all other orbitals are unoccupied). More precisely, for the present illustrative calculation, we have $n_{0s_{1/2}} \approx 0.96$ for the neutrons and $n_{0s_{1/2}} \approx 1.92$ for the protons. The next most occupied orbitals are the p -shell orbitals and the $1s_{1/2}$ orbital of the sd shell, with mean occupations of $\sim 10^{-2}$, while occupations fall off towards $\sim 10^{-3}$ and below for higher orbitals.

Overall, in Fig. 7, the general impression is that the natural orbitals simply “tweak” the oscillator radial functions, with modest shifts to the peak location and overall shape (again,

a linear scale does not do justice to changes in the asymptotics). The difference in proton and neutron structure in the reference many-body calculation for ${}^3\text{He}$ is manifest in the differences between corresponding proton and neutron natural orbitals. The distinction is most striking for the proton $0p_{3/2}$ orbital, which is shifted to markedly larger radii than the corresponding neutron orbital (which remains close to the underlying oscillator function). In general, the proton radial functions develop more pronounced tails than the neutron orbitals, visible even on a linear scale, suggestive of Coulomb repulsion effects.

In atomic and molecular electron structure theory, it is recognized that an important characteristic of the natural orbitals, including the unoccupied orbitals, is their tendency to remain localized in the region of high particle density [25]. This is to be contrasted with the unoccupied (virtual) Hartree-Fock orbitals, which instead provide an expansion of the continuum.

It is thus worth elaborating on an essential difference between natural orbitals and Hartree-Fock orbitals (*e.g.*, Ref. [42]). The unoccupied natural orbitals are well-defined, from the densities of the reference many-body calculation. In contrast, the basic variational condition for the Hartree-Fock ground state focuses entirely on optimizing the occupied orbitals, so as to minimize the energy in a single Slater determinant. The unoccupied orbitals are entirely unconstrained by this variational condition (except insofar as they must span an orthogonal complement to the occupied orbitals). The iterative calculational procedure for obtaining Hartree-Fock orbitals introduces a single-particle eigenproblem (involving Hartree and exchange potentials), intended to yield the occupied orbitals. While the set of solutions can be extended to provide a definition (one particular choice) for the unoccupied Hartree-Fock orbitals, it is not at all obvious that these unoccupied Hartree-Fock orbitals should be particularly well-suited for efficiently expanding the many-body wave functions in a configuration-interaction basis.

C. Center-of-mass factorization

A factorized and well-controlled center-of-mass motion is important, as discussed in Sec. IIB, if the results of the many-body calculation are to be of practical use, beyond limited calculations for ground-state observables. Recall that the N_{max} -truncated oscillator basis is special, in that the many-body wave functions resulting from NCCI calculations

with this basis factorize into intrinsic and center-of-mass parts, and the center-of-mass part can be selected to have pure oscillator $0s$ zero-point motion in the center-of-mass coordinate. Such exact factorization is no longer guaranteed, and no longer to be expected, if we move away from the N_{max} -truncated oscillator basis. However, approximate factorization may arise, with or without the persuasion of a Lawson term in the Hamiltonian. Let us therefore diagnose the center-of-mass motion which arises in our present calculations with the natural-orbital basis, and how it depends upon the choice of underlying oscillator basis.

For many purposes, we might be satisfied by factorization involving an arbitrary center-of-mass wave function. For instance, angular momentum selection rules which allow the intrinsic electromagnetic operators to be replaced with one-body operators in practical calculations [18] require factorization with an s -wave center-of-mass wave function, as $|\Psi_J\rangle = [|\Psi_J^{\text{intr}}\rangle \times |\Psi_{L_{\text{c.m.}}=0}^{\text{c.m.}}\rangle]_J$, but not specifically an oscillator $0s$ wave function. However, in practice, we do not have a good way to measure how well a many-body wave function factorizes, unless the factorization specifically involves $0s$ harmonic-oscillator motion.

Specifically, the expectation value of the center-of-mass number operator $N_{\text{c.m.}}$ allows us to measure deviations from pure $0s$ center-of-mass motion [20, 61–63]. Such $0s$ center-of-mass motion then incidentally implies factorization as $|\Psi_J\rangle = [|\Psi_J^{\text{intr}}\rangle \times |\Psi_{0s}^{\text{c.m.}}\rangle]_J$. The definition of a center-of-mass harmonic-oscillator number operator depends upon the oscillator parameter $\hbar\omega_{\text{c.m.}}$ taken for the center-of-mass motion:

$$\begin{aligned} N_{\text{c.m.}}(\hbar\omega_{\text{c.m.}}) &= \mathbf{c}_{\text{c.m.}}^\dagger \cdot \mathbf{c}_{\text{c.m.}} \\ &= \frac{1}{2}(\hbar\omega_{\text{c.m.}})^{-1} \frac{(\hbar c)^2}{A(m_N c^2)} K^2 + \frac{1}{2}(\hbar\omega_{\text{c.m.}}) \frac{A(m_N c^2)}{(\hbar c)^2} R^2 - \frac{3}{2}, \end{aligned} \quad (9)$$

where $\mathbf{c}_{\text{c.m.}}^\dagger$ and $\mathbf{c}_{\text{c.m.}}$ are the center-of-mass ladder operators (see Sec. F.3 of Ref. [18] for definitions), $K^2 = |\mathbf{k}_{\text{c.m.}}|^2$ is the squared magnitude of the center-of-mass momentum vector or, more precisely, wave vector, where $\mathbf{p}_{\text{c.m.}} = \hbar\mathbf{k}_{\text{c.m.}}$, and $R^2 = |\mathbf{x}_{\text{c.m.}}|^2$ is the squared magnitude of the center-of-mass coordinate vector [18]. Taking the expectation value of the expression in (9), we see that $\langle N_{\text{c.m.}}(\hbar\omega_{\text{c.m.}}) \rangle$ depends on the many-body wave function only through the two expectation values $\langle K^2 \rangle$ and $\langle R^2 \rangle$, which must then be taken in linear combination, weighted by the appropriate numerical coefficients from (9). These expectation values are readily evaluated within standard NCCI many-body codes, since R^2 and K^2 are simply scalar two-body operators, like the Hamiltonian itself.

Then $\langle N_{\text{c.m.}}(\hbar\omega_{\text{c.m.}}) \rangle$ vanishes if and only if the wave function has pure factorized

742 harmonic-oscillator 0s center-of-mass motion, corresponding to the given oscillator length. A
 743 nonvanishing $\langle N_{\text{c.m.}} \rangle$ measures, or at least places a limit upon, the deviation from such pure
 744 factorized 0s motion.¹⁰ In particular, the total contribution to the norm from components
 745 with nonzero excitation of the center-of-mass degree of freedom is $P(N_{\text{c.m.}} > 0) \leq \langle N_{\text{c.m.}} \rangle$.

746 However, as emphasized in Ref. [61], simply evaluating $\langle N_{\text{c.m.}}(\hbar\omega) \rangle$, with $\hbar\omega_{\text{c.m.}}$ taken
 747 as the $\hbar\omega$ of the underlying oscillator basis, will, in general, overestimate the center-of-
 748 mass contamination. Even if it so happens that the wave function obtained in an NCCI
 749 calculation, in some natural-orbital basis, factorizes (or approximately factorizes), with 0s
 750 oscillator motion for the center of mass, there is no reason to expect that the oscillator
 751 parameter for this center-of-mass motion will match that of the oscillator basis used in
 752 the original NCCI calculation which yielded the reference state from which the natural
 753 orbitals were derived. Rather, we must search for the value of $\hbar\omega_{\text{c.m.}}$ in (9) which minimizes
 754 $\langle N_{\text{c.m.}}(\hbar\omega_{\text{c.m.}}) \rangle$. This value, denoted by $\hbar\tilde{\omega}_{\text{c.m.}}$ (or simply $\hbar\tilde{\omega}$ in Ref. [61]), is readily extracted
 755 from (9) in analytic form, as

$$\hbar\tilde{\omega}_{\text{c.m.}} = \frac{(\hbar c)^2}{A(m_N c^2)} \left(\frac{\langle K^2 \rangle}{\langle R^2 \rangle} \right)^{1/2}, \quad (10)$$

756 and the corresponding minimized measure of the center-of-mass contamination, $\tilde{N}_{\text{c.m.}} \equiv$
 757 $\langle N_{\text{c.m.}}(\hbar\tilde{\omega}_{\text{c.m.}}) \rangle$, is given by

$$\tilde{N}_{\text{c.m.}} = (\langle K^2 \rangle \langle R^2 \rangle)^{1/2} - \frac{3}{2}. \quad (11)$$

758 With this in mind, let us now examine the center-of-mass motion for the ^3He ground
 759 state wave functions obtained in a natural-orbital basis. The values of $\langle N_{\text{c.m.}}(\hbar\omega_{\text{c.m.}}) \rangle$, as
 760 we sweep $\hbar\omega_{\text{c.m.}}$ in (9), are shown in Fig. 8. Each curve is simply determined analytically,
 761 by (9), taking the calculated $\langle K^2 \rangle$ and $\langle R^2 \rangle$ for the corresponding wave function. We again
 762 (as in Fig. 5) take $\hbar\omega = 9 \text{ MeV}$ [Fig. 8(a)], 15 MeV [Fig. 8(b)], and 25 MeV [Fig. 8(c)] as
 763 representative values for the oscillator parameter of the underlying oscillator basis (namely,
 764 below, near, and above the variational energy minimum, respectively).

¹⁰ In general, the many-body state $|\Psi\rangle$ may be decomposed into components with different eigenvalues of

$N_{\text{c.m.}}$: $|\Psi\rangle = \alpha_0|\Psi_{N_{\text{c.m.}}=0}\rangle + \alpha_1|\Psi_{N_{\text{c.m.}}=1}\rangle + \alpha_2|\Psi_{N_{\text{c.m.}}=2}\rangle + \dots$. Then $\langle N_{\text{c.m.}} \rangle = \sum_{\nu} \alpha_{\nu}^2 \nu$, which vanishes if
 and only if $|\Psi\rangle = |\Psi_{N_{\text{c.m.}}=0}\rangle$. This is simply the variational principle for the nonnegative-definite operator
 $N_{\text{c.m.}}$.

For $N_{\max} = 0$ (thick gray line), in Fig. 8, recall that the natural orbitals are simply the original oscillator functions, with oscillator parameter $\hbar\omega$, and calculations in the natural-orbital basis are simply calculations in the oscillator basis. The center-of-mass motion is thus pure $0s$ motion, with $\hbar\tilde{\omega}_{\text{c.m.}} = \hbar\omega$ (vertical dotted line), for which $\tilde{N}_{\text{c.m.}} = 0$. (In fact, curves identical to that shown would be obtained for any of the N_{\max} -truncated oscillator-basis calculations with this same $\hbar\omega$.)

Then, for the calculations in a natural-orbital basis proper, with $N_{\max} = 4$ (dotted line) through 16 (solid line), in Fig. 8, there is no $\hbar\omega_{\text{c.m.}}$ for which $\langle N_{\text{c.m.}} \rangle$ vanishes. Rather, the location of the minimum in $\langle N_{\text{c.m.}} \rangle$, given by (10) and (11), is marked by a dot.

For $\hbar\omega = 9 \text{ MeV}$ [Figs. 8(a)], there is an initial discontinuity going from the oscillator basis to a natural-orbital basis, where $\tilde{N}_{\text{c.m.}}$ jumps to $\gtrsim 10^{-2}$ for $N_{\max} = 4$, then steadily decreases again, converging to a value $\sim 10^{-3}$. The optimal $\hbar\omega_{\text{c.m.}}$ for recognizing this approximate factorization is $\hbar\tilde{\omega}_{\text{c.m.}} \approx 9.4 \text{ MeV}$, slightly above the $\hbar\omega$ of the underlying oscillator basis ($\hbar\omega = 9 \text{ MeV}$).

Moving to the other side of the variational minimum in $\hbar\omega$, for $\hbar\omega = 25 \text{ MeV}$ [Figs. 8(c)], there is again an initial discontinuity, with $\tilde{N}_{\text{c.m.}} \sim 10^{-2}$ for $N_{\max} = 4$, and converging towards $\gtrsim 10^{-3}$. Here the optimal $\hbar\omega_{\text{c.m.}}$ for recognizing this approximate factorization is $\hbar\tilde{\omega}_{\text{c.m.}} \approx 19 \text{ MeV}$, notably below the $\hbar\omega$ of the underlying oscillator basis ($\hbar\omega = 25 \text{ MeV}$).

Finally, for $\hbar\omega = 15 \text{ MeV}$ [Figs. 8(b)], near the variational energy minimum, after $\tilde{N}_{\text{c.m.}}$ initially jumps to $\tilde{N}_{\text{c.m.}} \lesssim 10^{-2}$ for $N_{\max} = 4$, it then immediately drops to $\tilde{N}_{\text{c.m.}} \approx 10^{-3}$ for higher N_{\max} . The location of the minimum drifts slightly downward, from the $\hbar\omega$ of the underlying oscillator basis ($\hbar\omega = 15 \text{ MeV}$), toward $\hbar\tilde{\omega}_{\text{c.m.}} \approx 12.5 \text{ MeV}$.

Thus, in each case, regardless of the $\hbar\omega$ for the underlying oscillator basis, a reasonably pure $0s$ center-of-mass motion spontaneously emerges for the ^3He ground state, as recognized when the appropriate choice $\hbar\tilde{\omega}_{\text{c.m.}}$ of oscillator parameter is used in measuring the center-of-mass motion, implying also a high degree of center-of-mass factorization. Furthermore, in each case, this $\hbar\tilde{\omega}_{\text{c.m.}}$ for which $0s$ motion is most closely realized differs from the $\hbar\omega$ of the underlying oscillator basis.

To more systematically map out the behaviors we have just seen, $\hbar\tilde{\omega}_{\text{c.m.}}$ and $\tilde{N}_{\text{c.m.}}$ are shown as functions of the underlying oscillator basis $\hbar\omega$ in Fig. 9. For large N_{\max} , the dependence of $\hbar\tilde{\omega}_{\text{c.m.}}$ on $\hbar\omega$ [Fig. 9(a)] is nearly linear, but of shallower slope than the reference line $\hbar\tilde{\omega}_{\text{c.m.}} = \hbar\omega$ (dashed diagonal line). The oscillator parameter $\hbar\tilde{\omega}_{\text{c.m.}}$ for the

center-of-mass motion matches that of the underlying oscillator basis for the natural orbitals in the vicinity of $\hbar\omega = 10 \text{ MeV}$ to 12.5 MeV . In this range of $\hbar\omega$, at high N_{max} , one also observes that the purest $0s$ center-of-mass motion is obtained [Fig. 9(b)], with $\tilde{N}_{\text{c.m.}} \lesssim 10^{-4}$.

A rough intuitive understanding of the center-of-mass motion, in particular, the behavior of the preferred $\hbar\tilde{\omega}_{\text{c.m.}}$ observed in Fig. 9(a), follows from the $\hbar\omega$ -dependence noted above for the natural orbitals themselves (Sec. III B). Recall the tendency, observed in Fig. 5, for natural orbitals obtained from a low- $\hbar\omega$ underlying oscillator basis [Fig. 5(a)] to still resemble oscillator orbitals, but of a somewhat higher $\hbar\omega$, closer to $\hbar\omega \approx 15 \text{ MeV}$, and for natural orbitals obtained from a high- $\hbar\omega$ underlying oscillator basis [Fig. 5(c)] to resemble oscillator orbitals of a somewhat lower $\hbar\omega$, again closer to $\hbar\omega \approx 15 \text{ MeV}$. To the extent that the low-lying natural orbitals resemble oscillator orbitals of some $\hbar\omega$, then a (nominally N_{max} -truncated) calculation in such a natural-orbital basis may be expected to have similar properties to an (N_{max} -truncated) calculation in an oscillator basis of this same $\hbar\omega$. It is thus perhaps not surprising that $\hbar\tilde{\omega}_{\text{c.m.}}$ of the center-of-mass wave function follows the same overall trend as the “effective” $\hbar\omega$ of the natural orbitals.

However, we must always keep in mind that $\langle N_{\text{c.m.}} \rangle$ is, strictly, only a measure of center-of-mass contamination, relative to harmonic-oscillator $0s$ motion, and therefore only incidentally provides an upper bound on the breakdown of center-of-mass factorization. Nonzero $\langle N_{\text{c.m.}} \rangle$ could reflect that factorization is broken, but it could also simply mean that we have factorization which is of a more difficult form to recognize, since the center-of-mass motion is not simply described by a $0s$ oscillator wave function.

Furthermore, for the present many-body calculations in the natural-orbital basis, recall that we have included no Lawson center-of-mass term (Sec. II) in the Hamiltonian. For now, we are thus identifying the center-of-mass motion which emerges spontaneously when we diagonalize a translationally-invariant intrinsic Hamiltonian, restricted to the particular truncated many-body space of these calculations. Starting from this baseline, one may then explore the effect of including a Lawson term, which is expected to refine the center-of-mass motion, at some cost to the convergence of the intrinsic motion (see Ref. [35] for initial examples of such calculations). Here one might more naturally choose an $\hbar\omega_{\text{c.m.}}$ parameter for the Lawson term which reinforces the center-of-mass motion as it already spontaneously emerges in the natural-orbital basis ($\hbar\omega_{\text{c.m.}} = \hbar\tilde{\omega}_{\text{c.m.}}$) rather than simply matching the oscillator parameter the underlying oscillator basis ($\hbar\omega_{\text{c.m.}} = \hbar\omega$).

IV. NATURAL ORBITALS AND HALO STRUCTURE: ${}^6\text{He}$

A. Convergence of observables

For a halo nucleus, such as ${}^6\text{He}$, the connection between natural orbitals and the single-particle structure of the nucleus should be particularly revealing. The natural orbitals occupied by halo nucleons may be expected to reflect the large-distance behavior which generates the halo. The ground state of ${}^6\text{He}$ is understood to be clusterized, consisting of a ${}^4\text{He}$ (or α) core plus two weakly-bound neutrons. This leads to a spatially-extended neutron distribution [88, 89], with possible correlations in the motion of the halo neutrons [39, 90–92]. The weak binding is reflected in a small two-neutron separation energy (≈ 0.97 MeV), while the extended spatial structure is reflected in a marked increase in r.m.s. radius observables from ${}^4\text{He}$ to ${}^6\text{He}$. Having already explored the basic properties of NCCI calculations in a natural-orbital basis for ${}^3\text{He}$ (Sec. III), we will take these as a baseline for comparison for ${}^6\text{He}$. Let us first consider the calculated energy and radius observables for ${}^6\text{He}$, with a natural-orbital basis, then (in the subsequent Sec. IIIB below) the radial wave functions of the orbitals themselves.

The ${}^6\text{He}$ ground state energy is shown in Fig. 10, as calculated with oscillator (solid circles) and natural-orbital (open squares) bases. Here we consider truncations through $N_{\text{max}} = 14$, again with the Daejeon16 interaction. The experimental binding energy [80] is shown for comparison (filled diamond).

The energy obtained with natural orbitals, in Fig. 10, is consistently lower than that obtained in the underlying oscillator basis, and is thus, by the variational principle, closer to the true energy in the full many-body space. In the vicinity of the variational minimum, the energy obtained with natural orbitals is approximately “one step” in N_{max} ahead of that obtained with oscillator orbitals. This relation strictly holds for the highest N_{max} shown in Fig. 10 (*i.e.*, the energy obtained in the natural-orbital basis for $N_{\text{max}} = 12$ lies below that obtained in the oscillator basis for $N_{\text{max}} = 14$). The $\hbar\omega$ dependence of the calculated energy is, again, much reduced in the natural-orbital basis, so the improvement of the natural-orbital results over the oscillator-basis results becomes more marked as we move away from the variational energy minimum and towards the extreme values of $\hbar\omega$ shown in Fig. 10.

Whereas for ${}^3\text{He}$ we could benchmark the calculated energies against an effectively con-

859 verged value obtained at much higher N_{\max} , as in Fig. 2(c), we no longer have this luxury
 860 for ${}^6\text{He}$, where the growth in dimension with N_{\max} is much more rapid (Fig. 1). We must
 861 simply compare the calculations obtained with oscillator and natural-orbital bases, and for
 862 different N_{\max} , against each other.

863 The overall scale of the change in calculated energy with N_{\max} for ${}^6\text{He}$ is much larger
 864 than for ${}^3\text{He}$. In the vicinity of the variational energy minimum, the change in calculated
 865 energy with each step in N_{\max} is $\lesssim 0.1 \text{ MeV}$ (Fig. 10), compared to steps of $\approx 0.001 \text{ MeV}$
 866 for comparable N_{\max} in ${}^3\text{He}$ (Fig. 2). This difference might be taken to reflect the greater
 867 complication in reproducing a higher- A system in general, as well as the challenging halo
 868 structure of ${}^6\text{He}$ in particular.

869 However, in judging convergence, what is important is not only the size of the change
 870 between values calculated with successive N_{\max} , but how this change decreases with N_{\max} .
 871 A convenient baseline against which to compare the convergence of the ground state energy
 872 is the hypothesis of exponential convergence with respect to N_{\max} ,

$$E(N_{\max}) = E_{\infty} + a \exp(-cN_{\max}), \quad (12)$$

873 where E_{∞} is then the full-space value [57]. The calculated values approach the full-space
 874 value in a geometric progression with successive steps in N_{\max} . For exponential convergence,
 875 the residual $\delta E(N_{\max}) \equiv E(N_{\max}) - E_{\infty}$ of the calculated energy relative to the full-space
 876 value, considered above for ${}^3\text{He}$ (Sec. III A), is given by $\delta E(N_{\max}) = a \exp(-cN_{\max})$, and
 877 thus decreases by a constant factor e^{-2c} with each (even) step in N_{\max} . On a logarithmic
 878 plot of the residual, as we considered for ${}^3\text{He}$ in Fig. 2(c), this appears as equally spaced
 879 steps with respect to N_{\max} , as was indeed approximately noted for ${}^3\text{He}$ (Sec. III A).

880 For ${}^6\text{He}$, we have no converged value with respect to which to take residuals, and thus
 881 cannot generate a logarithmic plot of residuals as in Fig. 2(c). Nonetheless, we can still
 882 compare successive calculated values of the energy, for successive truncations N_{\max} , and
 883 consider their difference $\Delta E(N_{\max}) = E(N_{\max}) - E(N_{\max} - 2)$. For exponential convergence,
 884 the ratio of successive steps

$$\eta(N_{\max}) \equiv \frac{E(N_{\max}) - E(N_{\max} - 2)}{E(N_{\max} - 2) - E(N_{\max} - 4)}, \quad (13)$$

885 is simply a constant $\eta = e^{-2c}$, independent of N_{\max} . That is, $\eta = 0.5$ corresponds to a
 886 step size in E which is halved with each successive step in N_{\max} , and a smaller value of η

corresponds to a more rapid exponential decay towards the full-space value. Such differences which decrease by a constant ratio again appear, on a logarithmic plot, to move downward by equal increments with each step in N_{\max} .

We thus consider a plot of $\log|\Delta E|$ for the ${}^6\text{He}$ ground state energy, in Fig. 11. The overall convergence behavior is qualitatively similar for calculations in oscillator (solid circles) and natural orbital (open squares) bases. The spacing between curves for successive N_{\max} is roughly uniform with N_{\max} , but decreases gradually for higher N_{\max} , *i.e.*, the convergence “slows down” relative to exponential convergence. For the energies calculated in either basis, the step size ΔE decreases by a factor of $\sim 0.4\text{--}0.6$ with each step in N_{\max} . At low N_{\max} , ΔE in either basis is roughly comparable. However, for high N_{\max} , the curves representing ΔE for the calculations in the natural-orbital basis lie approximately one step in N_{\max} ahead of those for the oscillator basis. Near the variational minimum in energy ($\hbar\omega \approx 15\text{ MeV}$), this is consistent with the observation from above, that the natural-orbital basis improves on the best oscillator-basis energy by about one step in N_{\max} . But this observation holds uniformly over a wide range extending to higher $\hbar\omega$, as well (at lower $\hbar\omega$, the ΔE obtained with the natural orbital basis falls off much more sharply with N_{\max}).

We now consider the r.m.s. radii, which provide measures of the halo structure. The calculated values of both r_p and r_n , for the ${}^6\text{He}$ ground state, are shown in Fig. 12. Note that the point-proton r.m.s. radius r_p , the point-neutron r.m.s. radius r_n , and the matter (or total point-nucleon) radius r_m form a redundant set of observables, related by $Ar_m^2 = Zr_p^2 + Nr_n^2$. It is thus worth briefly reviewing the physical significance of these observables, in the context of ${}^6\text{He}$ [21, 85].

Although r_p does not *directly* measure neutron halo structure, it is nonetheless *indirectly* sensitive to this structure, and it is accessible to electromagnetic measurement, through its simple relation to the charge radius. It is important to keep in mind that r_p , as calculated here and as accessed in experiment, is defined relative to the common center of mass of the protons and neutrons (see, *e.g.*, Refs. [6, 18, 21, 89]). In the cluster halo description of ${}^6\text{He}$, the α recoils against the halo neutrons, which consequently displaces the center of mass of the α (and thus of the protons) relative to this common center of mass. This induces an increase in r_p going from ${}^4\text{He}$ to ${}^6\text{He}$. (There may also be contributions from modifications to the structure of the α particle itself, or “core polarization” [85].) Experimentally, the increase in r_p from 1.462(6) fm for ${}^4\text{He}$ to 1.934(9) fm for ${}^6\text{He}$ [85, 93, 94] is taken as a

principal indicator of halo structure in ${}^6\text{He}$.

Then, both r_n and r_m include direct contributions from the halo neutrons. While r_n is more selectively a measure of the neutron distribution, it is r_m which is extracted from nuclear reaction cross section or proton-nucleus elastic scattering measurements. The results thereby obtained for the He isotopes are model-dependent and contradictory (see Sec. III A of Ref. [21] for an overview). They variously suggest $r_m \approx 2.3\text{ fm} - 2.7\text{ fm}$ in ${}^6\text{He}$, corresponding to an increase relative to ${}^4\text{He}$ of $\approx 50\% - 90\%$. Subject to these uncertainties, the increased matter radius in ${}^6\text{He}$ is again taken as an indicator of halo structure.

For the calculated r_p (lower curves in Fig. 12), the results obtained in the natural-orbital basis yield reduced $\hbar\omega$ dependence relative to those obtained in the oscillator basis, much as already seen for ${}^3\text{He}$ (Fig. 4). At the extremes in $\hbar\omega$ shown in Fig. 12, the calculations in the natural-orbital basis thus lie several steps in N_{max} “ahead” of the oscillator-basis calculations. Again, we show the value of r_p deduced from the experimental r_c [83] for comparison (filled diamond).

For ${}^6\text{He}$, the curves of radius *vs.* $\hbar\omega$ exhibit recognizable crossing points regardless of which basis is used. Recall (Sec. III A) that these crossing points have been suggested as a heuristic estimator of the full-space value. These crossing points are displaced in $\hbar\omega$ relative to each other — from $\hbar\omega \approx 10\text{ MeV}$ for the oscillator basis down to $\hbar\omega \approx 7\text{ MeV}$ for the natural-orbital basis — but occur at comparable values for the observable ($r_p \approx 1.9\text{ fm}$), consistent with the experimental value noted above.

Naturally, given the halo structure, the calculated values for r_n (upper curves in Fig. 12) are larger than for r_p , the $\hbar\omega$ dependence is stronger, and the changes in calculated value with each step in N_{max} is larger. Again, crossing points are obtained for calculations in both the oscillator and natural-orbital bases, shifted towards lower $\hbar\omega$ (longer oscillator length) than for r_p , namely $\hbar\omega \approx 9\text{ MeV}$ for the oscillator basis, and approaching $\hbar\omega \approx 6\text{ MeV}$ for the natural-orbital basis. This shift is perhaps not surprising given the larger radial extent of the structure being described. These two crossing points again occur at comparable values for r_n , in the range $r_n \approx 2.6\text{ fm} - 2.7\text{ fm}$. (In conjunction with the above value for r_p , this suggests $r_m \approx 2.4\text{ fm} - 2.5\text{ fm}$.) The highest N_{max} curves for the natural orbital calculations develop a flat “shoulder”, varying by $\lesssim 0.05\text{ fm}$ over several steps in $\hbar\omega$. This range of calculated r_n values is comparable with the range $r_n \approx 2.5\text{ fm} - 3.0\text{ fm}$ suggested by the range of experimental matter radii (discussed above) in conjunction with r_p .

951 The transformation to a natural-orbital basis clearly does not definitively solve the prob-
 952 lem of convergence for the r.m.s. radius observables. Nonetheless, it does contribute to
 953 taming the convergence behavior for these observables.

954 B. Natural orbitals

955 Turning to the natural orbitals themselves, the radial wave functions for the lowest natural
 956 orbitals are shown in Fig. 13, for a high- N_{max} calculation ($N_{\text{max}} = 14$) with $\hbar\omega$ near the
 957 variational energy minimum ($\hbar\omega = 15$ MeV). The orbitals shown again correspond, by their
 958 nlj labels, to the oscillator orbitals through the sd shell, as in the analogous figure above for
 959 ${}^3\text{He}$ (Fig. 7). Radial functions are shown for both protons (short dashed lines) and neutrons
 960 (long dashed lines), and the oscillator radial functions are again shown for comparison (thick
 961 gray lines).

962 The mean occupancies of these natural orbitals, indicated by the bars at top right in each
 963 panel of Fig. 13, are not far from what would be expected in a traditional shell model picture.
 964 The s shell is almost filled, with an occupancy of 1.81 for protons and 1.86 for neutrons.
 965 Most of the remaining occupancy, out of a total occupancy of 2 for the protons and 4 for the
 966 neutrons, lies in the p shell. For the neutrons, in particular, the $0p_{3/2}$ orbital, which would be
 967 the expected orbital for the two valence neutrons in an extreme noninteracting shell model
 968 picture, naturally enough has a mean occupancy of 1.81, while the $0p_{1/2}$ orbital accounts for
 969 a mean occupancy of 0.21. By contrast, the $1s_{1/2}$ orbital has a mean occupation of < 0.05 .
 970 Thus, the halo neutrons are decisively p -shell nucleons. The occupancies for the low-lying
 971 natural orbitals are higher than for the corresponding oscillator orbitals in the underlying
 972 calculation, but only marginally so: the increase in occupancy is by ≈ 0.16 for the neutron
 973 $p_{3/2}$ orbital, but only at the level of ≈ 0.01 for the remaining s -shell and p -shell orbitals, for
 974 both protons and neutrons.

975 The $0s_{1/2}$ natural orbitals appear virtually unchanged, in Fig. 13, relative to the underly-
 976 ing oscillator orbital, for both protons and neutrons. This is consistent with an unmodified
 977 α “core”. However, to examine the large-distance behavior, we turn to logarithmic plots,
 978 shown in Fig. 14. Intriguingly, while both the proton and neutron natural orbitals have lin-
 979 ear tails on the logarithmic plot, indicating exponential fall-off, the decay constants differ,
 980 with a slower fall-off (longer tail) for the neutron orbital.

981 The $0p_{3/2}$ orbital is of course of special interest, as the orbital “occupied” by the halo
 982 neutrons. The peak of the probability distribution, in the central region (Fig. 13), shifts
 983 only marginally outward in the radial coordinate, on the scale of ≈ 0.1 fm. But the tail
 984 is noticeably extended even viewed on a linear scale. This is confirmed as a shallow expo-
 985 nential fall-off when viewed on a logarithmic scale (Fig. 14). In contrast, the peak for the
 986 “unoccupied” proton $0p_{3/2}$ orbital moves to smaller radius, by a comparable amount, and
 987 the tail similarly is retracted (Fig. 13), with a much steeper exponential fall-off (Fig. 14).
 988 Similar observations hold for the $0p_{1/2}$ orbital, which, as noted above, is partially occupied
 989 by the valence neutrons.

990 The sd -shell orbitals are notionally “unoccupied” orbitals for both the protons and neu-
 991 trons. The mean occupations of these orbitals are each $\lesssim 0.05$. The proton orbitals move
 992 radially inward, relative to the oscillator orbital, both in terms of peak location and tail
 993 extent (Fig. 13). For the neutrons, the behavior is less consistent. The second peak of the
 994 $1s_{1/2}$ orbital, as well as the peak of the $0d_{5/2}$ orbital, both move markedly outwards, by
 995 ≈ 1 fm, and the tails of these orbitals are even more exaggeratedly extended than for the
 996 neutron p -shell orbitals. Yet the neutron $0d_{3/2}$ orbital has a behavior which closely resembles
 997 that of the corresponding proton orbital, in the central region at least. Asymptotically, the
 998 proton orbitals have similar exponential tails, with faster decay than the neutron orbitals
 999 (Fig. 14).

1000 For a “core” orbital, the proton $0s_{1/2}$ orbital, we explore the dependence on the $\hbar\omega$ and
 1001 N_{\max} of the reference calculation in Fig. 15. The sensitivity of the natural orbital to the
 1002 spectator $0s$ motion of the center of mass degree of freedom is similar to that already seen
 1003 for this same orbital in ${}^3\text{He}$, discussed in Sec. III B. Once again, convergence is rapidly
 1004 reached with increasing N_{\max} for the reference oscillator-basis calculation, while the shape
 1005 of this converged natural orbital is dependent upon the $\hbar\omega$ of the underlying oscillator-
 1006 basis calculation, which determines the $\hbar\omega_{\text{c.m.}}$ of the center-of-mass zero-point motion. In
 1007 ${}^6\text{He}$ (Fig. 15), the peak location for the natural orbital depends on the $\hbar\omega$ of the reference
 1008 calculation less strongly than for ${}^3\text{He}$ (Fig. 5), especially at low $\hbar\omega$.

1009 Then, for the principal “halo” orbital, the neutron $0p_{3/2}$ orbital, the $\hbar\omega$ and N_{\max} depen-
 1010 dence is similarly explored in Fig. 16, now on a logarithmic scale. (The peak location has
 1011 a similar dependence to that noted above for the proton $0s_{1/2}$ orbital.) The $\hbar\omega = 9$ MeV
 1012 oscillator basis [Fig. 16(a)], with its comparatively long oscillator length, provides the best

support in the tail region, and thus the fastest realization of a region of exponential decay (again, indicated by a straight line on the logarithmic plot). In contrast, the $\hbar\omega = 25$ MeV basis [Fig. 16(c)] yields the slowest grow-in of the exponential tail.

Finally, there is the question of the center-of-mass motion which emerges in these calculations for ${}^6\text{He}$ in a natural-orbital basis. We apply the same diagnostics for ${}^6\text{He}$, shown in Fig. 17, as considered earlier for ${}^3\text{He}$ in Sec. III C. That is, starting from the natural orbitals obtained from a reference oscillator basis calculation of given $\hbar\omega$, we carry out the many-body calculation for ${}^6\text{He}$, then evaluate the center-of-mass $\langle R^2 \rangle$ and $\langle K^2 \rangle$ observables. From these, we deduce the “optimal” value of the $\hbar\omega_{\text{c.m.}}$ parameter for center-of-mass motion, $\hbar\tilde{\omega}_{\text{c.m.}}$, such that the expectation value $\langle N_{\text{c.m.}} \rangle$ of the center-of-mass number operator assumes its minimum value $\tilde{N}_{\text{c.m.}}$.

Comparing the ${}^6\text{He}$ results for the center-of-mass diagnostics (Fig. 17) to the ${}^3\text{He}$ results (Fig. 9), a few features stand out. The dependence of both $\hbar\tilde{\omega}_{\text{c.m.}}$ [Fig. 17(a)] and $\tilde{N}_{\text{c.m.}}$ [Fig. 17(b)] on the reference basis parameters $\hbar\omega$ and N_{max} is generally smoother for ${}^6\text{He}$ than for ${}^3\text{He}$. The zig-zagging irregularities of Fig. 9 are no longer in evidence.

The oscillator parameter $\hbar\tilde{\omega}_{\text{c.m.}}$ for the center-of-mass motion [Fig. 17(a)] again matches that of the underlying oscillator basis for the natural orbitals in the vicinity of $\hbar\omega = 10$ MeV to 12.5 MeV. However, the $\hbar\omega$ dependence of $\hbar\tilde{\omega}_{\text{c.m.}}$ is less steep, above this point, for ${}^6\text{He}$ than for ${}^3\text{He}$ and, indeed, is continuing to become shallower with increasing N_{max} .

Furthermore, $\tilde{N}_{\text{c.m.}}$ [Fig. 17(b)] is comparatively independent of $\hbar\omega$. By $N_{\text{max}} = 14$, $\tilde{N}_{\text{c.m.}}$ has decreased to $\approx 10^{-3}$ over most of the $\hbar\omega$ range shown, and it continues to decrease with increasing N_{max} . Thus, in short, for practical purposes, a near-pure harmonic-oscillator 0s center-of-mass motion is uniformly obtained in the many-body calculations for ${}^6\text{He}$ in the natural-orbital basis.

V. CONCLUSION

The nuclear many-body system is highly correlated, and thus inherently requires many antisymmetrized product states (Slater determinants) for its accurate description. No choice of single-particle states can completely obviate the need for superposing antisymmetrized product states in representing a correlated system. Nonetheless, a judicious choice of single-particle basis can accelerate the convergence of the description of the many-body wave

1043 function in a configuration-interaction basis.

1044 Natural orbitals, obtained by diagonalizing the (scalar) one-body density matrix, address
 1045 this aim in a well-defined sense, by maximizing the occupation of low-lying orbitals, or
 1046 minimizing the depletion of the Fermi sea, in the expansion of a specific many-body reference
 1047 state. After outlining the procedure for constructing and using natural orbitals within the
 1048 NCCI framework (Sec. II), we have examined in detail the properties both of the orbitals
 1049 themselves and the consequent many-body calculations in a natural orbital basis, first for
 1050 the simple testbed case of ^3He (Sec. III), then for the halo nucleus ^6He (Sec. IV).

1051 There are several noteworthy factors (Sec. II) limiting what we might expect to accom-
 1052 plish, in practice, with the natural orbital basis in NCCI calculations. The natural orbitals
 1053 are only known to limited accuracy, as they are obtained from a reference many-body state
 1054 which is only an approximation to the true solution of the many-body problem (as it would
 1055 be obtained in an untruncated space). This reference state is represented in terms of or-
 1056 bitals from a truncated single-particle space, which limits the portion of the single-particle
 1057 space which the natural orbitals can sample. Moreover, the many-body space in which the
 1058 reference state is calculated is then subjected to a nontrivial truncation (*e.g.*, by N_{max}),
 1059 which may be expected to further restrict the fidelity of the reference state found therein
 1060 and, specifically, the representation of high-lying orbitals in the scalar density obtained from
 1061 this reference state.

1062 Furthermore, even if the reference state could be found exactly, and its natural orbitals
 1063 deduced exactly, one-body densities obtained from a laboratory-frame reference state are not
 1064 uniquely defined by the intrinsic structure. Rather, they reflect some spectator center-of-
 1065 mass motion arbitrarily superposed on this intrinsic structure. The natural orbitals obtained
 1066 from these densities are then used in a many-body calculation which, although intended
 1067 simply to reproduce the intrinsic structure of interest, in practice must yield some possibly
 1068 complicated combination of intrinsic and center-of-mass motion.

1069 Nonetheless, changing to a many-body basis constructed from natural orbitals does per-
 1070 mit an NCCI calculation to probe portions of the many-body space which were not acces-
 1071 sible in the original reference calculation. If the initial calculation is in an N_{max} -truncated
 1072 harmonic oscillator basis, as here, then the calculation in a natural orbital basis brings in
 1073 highly-excited oscillator configurations which were beyond the limit of the initial calculation.

1074 We find that the transformation from harmonic oscillator orbitals to natural orbitals

serves in part to simply accomplish a dilation of the harmonic oscillator basis, from the length scale (or $\hbar\omega$) of the underlying basis, to a more optimal length scale (or $\hbar\omega$). This observation (*e.g.*, Fig. 15) already explains the relative insensitivity of calculated energies and other observables in a natural orbital basis to the $\hbar\omega$ of the underlying oscillator basis: as one varies $\hbar\omega$, the transformation to natural orbitals simply undoes this variation. Such dilation, in itself, merely recovers the results of a harmonic oscillator basis chosen with optimal length scale, rather than improving on it.

More substantially, though, the transformation to natural orbitals provides genuine modifications to the shape of the radial wave functions. Notably, the artificial Gaussian fall-off of the oscillator functions is modified to more closely resemble the exponential fall-off physically expected from the finite range of the nuclear interaction (*e.g.*, Fig. 14). These differences can account for the improvements over the results obtained, even with an optimal choice of $\hbar\omega$, using the harmonic oscillator basis.

In the present work, where we retain the convenient but simpleminded “nominal N_{\max} ” truncation scheme (Sec. II B) for the many-body basis generated from the natural orbitals, we find improvements by about one step in N_{\max} over the oscillator-basis calculations. (Although illustrated here for the Daejeon16 interaction, similar results are found with other interactions, *e.g.*, in the preliminary study [34, 35] with JISP16.) While this improvement is incremental, it is nonetheless welcome. The computational cost of a second calculation (with natural orbitals) in a space of the same dimension as the underlying reference calculation (with oscillator orbitals) is typically far less than that of performing a new calculation in a space of higher N_{\max} , which typically entails an order-of-magnitude increase in dimension (Fig. 1), and correspondingly larger increase in memory demands and computational load [95].

However, the present exploration is also intended to provide a baseline for understanding more sophisticated many-body calculations based on natural orbitals derived from NCCI reference calculations. Here we reiterate that the eigenvalues of the density matrix provide information on the “importance” of orbitals, which could ostensibly be used to good effect in defining a weighting scheme for the many-body truncation. Moreover, natural orbitals provide a reasonable starting point [37] for hybrid many-body calculations which incorporate truncated configuration-interaction bases for portions of the calculation, *e.g.*, in-medium NCSM [96] and perturbatively-improved NCSM [97] calculations.

ACKNOWLEDGMENTS

We thank Guillaume Hupin for valuable discussions on the formulation of the nuclear natural orbital problem, Mitch A. McNanna for carrying out informative preliminary studies in one dimension, and Jakub Herko, Anna E. McCoy, Charlotte M. Wood, and Zhou Zhou for comments on the manuscript. This material is based upon work supported by the U.S. Department of Energy, Office of Science, under Award Numbers DE-FG02-95ER-40934, DE-FG02-91ER-40608, DE-SC0018223 (SciDAC4/NUCLEI), and DE-FG02-87ER40371. This research used computational resources of the University of Notre Dame Center for Research Computing and of the National Energy Research Scientific Computing Center (NERSC), a U.S. Department of Energy, Office of Science, user facility supported under Contract DE-AC02-05CH11231.

-
- [1] P. Navrátil, J. P. Vary, and B. R. Barrett, Properties of ^{12}C in the *ab initio* nuclear shell model, Phys. Rev. Lett. **84**, 5728 (2000).
 - [2] S. C. Pieper, R. B. Wiringa, and J. Carlson, Quantum Monte Carlo calculations of excited states in $A = 6-8$ nuclei, Phys. Rev. C **70**, 054325 (2004).
 - [3] T. Neff and H. Feldmeier, Cluster structures within fermionic molecular dynamics, Nucl. Phys. A **738**, 357 (2004).
 - [4] G. Hagen, D. J. Dean, M. Hjorth-Jensen, T. Papenbrock, and A. Schwenk, Benchmark calculations for ^3H , ^4He , ^{16}O , and ^{40}Ca with *ab initio* coupled-cluster theory, Phys. Rev. C **76**, 044305 (2007).
 - [5] S. Quaglioni and P. Navrátil, *Ab initio* many-body calculations of nucleon-nucleus scattering, Phys. Rev. C **79**, 044606 (2009).
 - [6] S. Bacca, N. Barnea, and A. Schwenk, Matter and charge radii of ^6He in the hyperspherical-harmonics approach, Phys. Rev. C **86**, 034321 (2012).
 - [7] N. Shimizu, T. Abe, Y. Tsunoda, Y. Utsuno, T. Yoshida, T. Mizusaki, M. Honma, and T. Otsuka, New-generation Monte Carlo shell model for the K computer era, Prog. Exp. Theor. Phys. **2012**, 01A205 (2012).
 - [8] T. Dytrych, K. D. Launey, J. P. Draayer, P. Maris, J. P. Vary, E. Saule, U. Catalyurek,

- 1135 M. Sosonkina, D. Langr, and M. A. Caprio, Collective modes in light nuclei from first princi-
 1136 ples, Phys. Rev. Lett. **111**, 252501 (2013).
- 1137 [9] B. R. Barrett, P. Navrátil, and J. P. Vary, *Ab initio* no core shell model, Prog. Part. Nucl.
 1138 Phys. **69**, 131 (2013).
- 1139 [10] S. Baroni, P. Navrátil, and S. Quaglioni, Unified *ab initio* approach to bound and unbound
 1140 states: No-core shell model with continuum and its application to ${}^7\text{He}$, Phys. Rev. C **87**,
 1141 034326 (2013).
- 1142 [11] R. B. Wiringa, V. G. J. Stoks, and R. Schiavilla, Accurate nucleon-nucleon potential with
 1143 charge-independence breaking, Phys. Rev. C **51**, 38 (1995).
- 1144 [12] D. R. Entem and R. Machleidt, Accurate charge-dependent nucleon-nucleon potential at fourth
 1145 order of chiral perturbation theory, Phys. Rev. C **68**, 041001(R) (2003).
- 1146 [13] A. M. Shirokov, J. P. Vary, A. I. Mazur, and T. A. Weber, Realistic nuclear Hamiltonian: *Ab*
 1147 *exitu* approach, Phys. Lett. B **644**, 33 (2007).
- 1148 [14] E. Epelbaum, H.-W. Hammer, and U.-G. Meißner, Modern theory of nuclear forces, Rev.
 1149 Mod. Phys. **81**, 1773 (2009).
- 1150 [15] T. Helgaker, P. Jørgensen, and J. Olsen, *Molecular Electron-Structure Theory* (Wiley, Chich-
 1151 ester, 2000).
- 1152 [16] M. Moshinsky and Y. F. Smirnov, *The Harmonic Oscillator in Modern Physics* (Harwood
 1153 Academic Publishers, Amsterdam, 1996).
- 1154 [17] J. P. Elliott and T. H. R. Skyrme, Centre-of-mass effects in the nuclear shell-model, Proc. R.
 1155 Soc. London A **232**, 561 (1955).
- 1156 [18] M. A. Caprio, A. E. McCoy, and P. J. Fasano, Intrinsic operators for the translationally-
 1157 invariant many-body problem, J. Phys. G **47**, 122001 (2020).
- 1158 [19] K. T. R. Davies, S. J. Krieger, and M. Baranger, A study of the Hartree-Fock approximation
 1159 as applied to finite nuclei, Nucl. Phys. **84**, 545 (1966).
- 1160 [20] M. A. Caprio, P. Maris, and J. P. Vary, The Coulomb-Sturmian basis for the nuclear many-
 1161 body problem, Phys. Rev. C **86**, 034312 (2012).
- 1162 [21] M. A. Caprio, P. Maris, and J. P. Vary, Halo nuclei ${}^6\text{He}$ and ${}^8\text{He}$ with the Coulomb-Sturmian
 1163 basis, Phys. Rev. C **90**, 034305 (2014).
- 1164 [22] P.-O. Löwdin, Quantum theory of many-particle systems. I. Physical interpretations by means
 1165 of density matrices, natural spin-orbitals, and convergence problems in the method of config-

- 1166 uration interaction, Phys. Rev. **97**, 1474 (1955).
- 1167 [23] H. Shull and P.-O. Löwdin, Natural spin orbitals for helium, J. Chem. Phys. **23**, 1565 (1955).
- 1168 [24] P.-O. Löwdin and H. Shull, Natural orbitals in the quantum theory of two-electron systems,
1169 Phys. Rev. **101**, 1730 (1956).
- 1170 [25] E. R. Davidson, Properties and uses of natural orbitals, Rev. Mod. Phys. **44**, 451 (1972).
- 1171 [26] C. Mahaux and R. Sartor, Single-particle motion in nuclei, in *Adv. Nucl. Phys.*, Vol. 20, edited
1172 by J. W. Negele and E. Vogt (Springer, Boston, 1991) p. 1.
- 1173 [27] G. A. Lalazissis, S. E. Massen, and C. P. Panos, Systematic study of the effect of short range
1174 correlations on the occupation numbers of the shell model orbits in light nuclei, Phys. Rev. C
1175 **46**, 201 (1992).
- 1176 [28] M. V. Stoitsov, A. N. Antonov, and S. S. Dimitrova, Natural orbital representation in nuclei,
1177 Phys. Rev. C **47**, R455 (1993).
- 1178 [29] M. V. Stoitsov, A. N. Antonov, and S. S. Dimitrova, Natural orbital representation and short-
1179 range correlations in nuclei, Phys. Rev. C **48**, 74 (1993).
- 1180 [30] I. J. Shin, Y. Kim, P. Maris, J. P. Vary, C. Forssén, J. Rotureau, and N. Michel, *Ab initio*
1181 no-core solutions for ${}^6\text{Li}$, J. Phys. G **44**, 075103 (2017).
- 1182 [31] Y. Jaganathen, R. M. Id Betan, N. Michel, W. Nazarewicz, and M. Płoszajczak, Quantified
1183 Gamow shell model interaction for *psd*-shell nuclei, Phys. Rev. C **96**, 054316 (2017).
- 1184 [32] P.-O. Löwdin, Expansion theorems for the total wave function and extended Hartree-Fock
1185 schemes, Rev. Mod. Phys. **32**, 328 (1960).
- 1186 [33] D. H. Kobe, Natural orbitals, divergences, and variational principles, J. Chem. Phys. **50**, 5183
1187 (1969).
- 1188 [34] Ch. Constantinou, M. A. Caprio, J. P. Vary, and P. Maris, *Ab initio* properties of the halo
1189 nucleus ${}^6\text{He}$ in a natural orbital basis, Nucl. Sci. Techniques **28**, 179 (2017).
- 1190 [35] Ch. Constantinou, *Natural orbitals for the no-core configuration interaction approach*, Ph.D.
1191 thesis, University of Notre Dame (2017).
- 1192 [36] G. Puddu, Many-body calculations with deuteron based single-particle bases and their asso-
1193 ciated natural orbits, Physica Scripta **93**, 065301 (2018).
- 1194 [37] A. Tichai, J. Müller, K. Vobig, and R. Roth, Natural orbitals for *ab initio* no-core shell model
1195 calculations, Phys. Rev. C **99**, 034321 (2019).
- 1196 [38] J. Hoppe, A. Tichai, M. Heinz, K. Hebeler, and A. Schwenk, Natural orbitals for many-body

- expansion methods, Phys. Rev. C **103**, 014321 (2021).
- [39] C. Robin, M. J. Savage, and N. Pillet, Entanglement rearrangement in self-consistent nuclear structure calculations, Phys. Rev. C **103**, 034325 (2021).
- [40] A. M. Shirokov, I. J. Shin, Y. Kim, M. Sosonkina, P. Maris, and J. P. Vary, N3LO NN interaction adjusted to light nuclei in *ab initio* approach, Phys. Lett. B **761**, 87 (2016).
- [41] P. Maris, I. J. Shin, and J. P. Vary, *Ab initio* structure of p -shell nuclei with chiral effective field theory and Daejeon16 interactions, in *Proceedings of the International Conference Nuclear Theory in the Supercomputing Era 2018*, edited by A. M. Shirokov and A. I. Mazur (Pacific National University, Khabarovsk, Russia, 2019) p. 168.
- [42] P. Ring and P. Schuck, *The Nuclear Many-Body Problem* (Springer-Verlag, New York, 1980).
- [43] A. J. Coleman and V. I. Yukalov, *Reduced Density Matrices*, Lecture Notes in Chemistry, Vol. 72 (Springer, Berlin, 2000).
- [44] R. McWeeny and W. Kutzelnigg, Symmetry properties of natural orbitals and geminals I. Construction of spin- and symmetry-adapted functions, Int. J. Quantum. Chem. **2**, 187 (1968).
- [45] J. Suhonen, *From Nucleons to Nucleus* (Springer-Verlag, Berlin, 2007).
- [46] J. J. Sakurai, *Modern Quantum Mechanics*, rev. ed., edited by S. F. Tuan (Addison-Wesley, Reading, Massachusetts, 1994).
- [47] P. A. M. Dirac, Note on exchange phenomena in the Thomas atom, Math. Proc. Cambridge Phil. Soc. **26**, 376 (1930).
- [48] K. Fan, On a theorem of Weyl concerning eigenvalues of linear transformations I, Proc. Nat. Acad. Sci. USA **35**, 652 (1949).
- [49] R. R. Whitehead, A. Watt, B. J. Cole, and I. Morrison, Computational methods for shell-model calculations, Adv. Nucl. Phys. **9**, 123 (1977).
- [50] A. R. Edmonds, *Angular Momentum in Quantum Mechanics*, 2nd ed., Investigations in Physics No. 4 (Princeton University Press, Princeton, New Jersey, 1960).
- [51] D. J. Rowe and J. L. Wood, *Fundamentals of Nuclear Models: Foundational Models* (World Scientific, Singapore, 2010).
- [52] H. A. Bethe and M. E. Rose, Kinetic energy of nuclei in the Hartree model, Phys. Rev. **51**, 283 (1937).
- [53] P. J. Brussaard and P. W. M. Glaudemans, *Shell-Model Applications in Nuclear Spectroscopy* (North-Holland Publishing Company, Amsterdam, 1977).

- [54] D. H. Gloeckner and R. D. Lawson, Spurious center-of-mass motion, Phys. Lett. B **53**, 313 (1974).
- [55] R. D. Lawson, *Theory of the Nuclear Shell Model* (Clarendon Press, Oxford, 1980).
- [56] A. M. Lane, Reduced widths of individual nuclear energy levels, Rev. Mod. Phys. **32**, 519 (1960).
- [57] S. K. Bogner, R. J. Furnstahl, P. Maris, R. J. Perry, A. Schwenk, and J. Vary, Convergence in the no-core shell model with low-momentum two-nucleon interactions, Nucl. Phys. A **801**, 21 (2008).
- [58] P. Maris and J. P. Vary, *Ab initio* nuclear structure calculations of *p*-shell nuclei with JISP16, Int. J. Mod. Phys. E **22**, 1330016 (2013).
- [59] M. A. Caprio, P. Maris, J. P. Vary, and R. Smith, Collective rotation from *ab initio* theory, Int. J. Mod. Phys. E **24**, 1541002 (2015).
- [60] M. A. Caprio, P. J. Fasano, P. Maris, and A. E. McCoy, Quadrupole moments and proton-neutron structure in *p*-shell mirror nuclei, Phys. Rev. C **104**, 034319 (2021).
- [61] G. Hagen, T. Papenbrock, and D. J. Dean, Solution of the center-of-mass problem in nuclear structure calculations, Phys. Rev. Lett. **103**, 062503 (2009); G. Hagen, T. Papenbrock, D. J. Dean, and M. Hjorth-Jensen, *Ab initio* coupled-cluster approach to nuclear structure with modern nucleon-nucleon interactions, Phys. Rev. C **82**, 034330 (2010).
- [62] R. Roth, J. R. Gour, and P. Piecuch, Center-of-mass problem in truncated configuration interaction and coupled-cluster calculations, Phys. Lett. B **679**, 334 (2009).
- [63] H. Hergert, S. K. Bogner, T. D. Morris, A. Schwenk, and K. Tsukiyama, The in-medium similarity renormalization group: A novel *ab initio* method for nuclei, Phys. Rep. **621**, 165 (2016).
- [64] H. Shull and P.-O. Löwdin, Role of the continuum in superposition of configurations, J. Chem. Phys. **23**, 1362 (1955).
- [65] E. J. Weniger, Weakly convergent expansions of a plane wave and their use in Fourier integrals, J. Math. Phys. **26**, 276 (1985).
- [66] A. E. McCoy and M. A. Caprio, Algebraic evaluation of matrix elements in the Laguerre function basis, J. Math. Phys. **57**, 021708 (2016).
- [67] J. W. Negele and H. Orland, *Quantum Many-Particle Systems* (Addison-Wesley, Redwood City, CA, 1988).

- [68] T. Abe, P. Maris, T. Otsuka, N. Shimizu, Y. Utsuno, and J. P. Vary, Benchmarks of the full configuration interaction, Monte Carlo shell model, and no-core full configuration methods, Phys. Rev. C **86**, 054301 (2012).
- [69] T. Dytrych, K. D. Sviratcheva, J. P. Draayer, C. Bahri, and J. P. Vary, *Ab initio* symplectic no-core shell model, J. Phys. G **35**, 123101 (2008).
- [70] J. P. Vary, P. Maris, P. J. Fasano, and M. A. Caprio, Perspectives on nuclear structure and scattering with the *ab initio* no-core shell model, JPS Conf. Proc. **23**, 012001 (2018).
- [71] R. Roth and P. Navrátil, *Ab initio* study of ^{40}Ca with an importance-truncated no-core shell model, Phys. Rev. Lett. **99**, 092501 (2007).
- [72] C. Lanczos, An iteration method for the solution of the eigenvalue problem of linear differential and integral operators, J. Res. Natl. Bur. Stand. (U. S.) **45**, 255 (1950).
- [73] M. L. Goldberger and K. M. Watson, *Collision Theory* (Wiley, New York, 1964).
- [74] P. Navrátil, Translationally invariant matrix elements of general one-body operators, Phys. Rev. C **104**, 064322 (2021), arXiv:2109.04017 [nucl-th].
- [75] G. Hagen, M. Hjorth-Jensen, and N. Michel, Gamow shell model and realistic nucleon-nucleon interactions, Phys. Rev. C **73**, 064307 (2006).
- [76] S. K. Bogner, R. J. Furnstahl, and R. J. Perry, Similarity renormalization group for nucleon-nucleon interactions, Phys. Rev. C **75**, 061001(R) (2007).
- [77] H. M. Aktulga, C. Yang, E. G. Ng, P. Maris, and J. P. Vary, Improving the scalability of symmetric iterative eigensolver for multi-core platforms, Concurrency Computat.: Pract. Exper. **26**, 2631 (2013).
- [78] M. Shao, H. M. Aktulga, C. Yang, E. G. Ng, P. Maris, and J. P. Vary, Accelerating nuclear configuration interaction calculations through a preconditioned block iterative eigensolver, Comput. Phys. Commun. **222**, 1 (2018).
- [79] M. A. Caprio and P. J. Fasano, computer code library **shell**.
- [80] M. Wang, W. Huang, F. Kondev, G. Audi, and S. Naimi, The AME 2020 atomic mass evaluation (II). Tables, graphs and references, Chin. Phys. C **45**, 030003 (2021).
- [81] C. Forssen, J. P. Vary, E. Caurier, and P. Navratil, Converging sequences in the *ab-initio* no-core shell model, Phys. Rev. C **77**, 024301 (2008).
- [82] P. Maris, J. P. Vary, and A. M. Shirokov, *Ab initio* no-core full configuration calculations of light nuclei, Phys. Rev. C **79**, 014308 (2009).

- [83] I. Angeli and K. P. Marinova, Table of experimental nuclear ground state charge radii: An update, *At. Data Nucl. Data Tables* **99**, 69 (2013).
- [84] J. L. Friar, J. Martorell, and D. W. L. Sprung, Nuclear sizes and the isotope shift, *Phys. Rev. A* **56**, 4579 (1997).
- [85] Z.-T. Lu, P. Mueller, G. W. F. Drake, W. Nörtershäuser, S. C. Pieper, and Z.-C. Yan, Laser probing of neutron-rich nuclei in light atoms, *Rev. Mod. Phys.* **85**, 1383 (2013).
- [86] A. Nogga, P. Navrátil, B. R. Barrett, and J. P. Vary, Spectra and binding energy predictions of chiral interactions for ${}^7\text{Li}$, *Phys. Rev. C* **73**, 064002 (2006).
- [87] C. Cockrell, J. P. Vary, and P. Maris, Lithium isotopes within the *ab initio* no-core full configuration approach, *Phys. Rev. C* **86**, 034325 (2012).
- [88] B. Jonson, Light dripline nuclei, *Phys. Rep.* **389**, 1 (2004).
- [89] I. Tanihata, H. Savajols, and R. Kanungo, Recent experimental progress in nuclear halo structure studies, *Prog. Part. Nucl. Phys.* **68**, 215 (2013).
- [90] S. Quaglioni, C. Romero-Redondo, and P. Navrátil, Three-cluster dynamics within an *ab initio* framework, *Phys. Rev. C* **88**, 034320 (2013).
- [91] D. Sääf and C. Forssén, Microscopic description of translationally invariant core+ n + n overlap functions, *Phys. Rev. C* **89**, 011303(R) (2014).
- [92] C. Romero-Redondo, S. Quaglioni, P. Navrátil, and G. Hupin, How many-body correlations and α clustering shape ${}^6\text{He}$, *Phys. Rev. Lett.* **117**, 222501 (2016).
- [93] L.-B. Wang, P. Mueller, K. Bailey, G. W. F. Drake, J. P. Greene, D. Henderson, R. J. Holt, R. V. F. Janssens, C. L. Jiang, Z.-T. Lu, T. P. O'Connor, R. C. Pardo, K. E. Rehm, J. P. Schiffer, and X. D. Tang, Laser spectroscopic determination of the ${}^6\text{He}$ nuclear charge radius, *Phys. Rev. Lett.* **93**, 142501 (2004).
- [94] M. Brodeur, T. Brunner, C. Champagne, S. Ettenauer, M. J. Smith, A. Lapierre, R. Ringle, V. L. Ryjkov, S. Bacca, P. Delheij, G. W. F. Drake, D. Lunney, A. Schwenk, and J. Dilling, First direct mass measurement of the two-neutron halo nucleus ${}^6\text{He}$ and improved mass for the four-neutron halo ${}^8\text{He}$, *Phys. Rev. Lett.* **108**, 052504 (2012).
- [95] P. Maris, H. M. Aktulga, S. Binder, A. Calci, Ü. V. Çatalyürek, J. Langhammer, E. Ng, E. Saule, R. Roth, J. P. Vary, and C. Yang, No core CI calculations for light nuclei with chiral 2- and 3-body forces, *J. Phys. Conf. Ser.* **454**, 012063 (2013).
- [96] E. Gebrerufael, K. Vobig, H. Hergert, and R. Roth, *Ab initio* description of open-shell nuclei:

- 1321 Merging no-core shell model and in-medium similarity renormalization group, Phys. Rev. Lett.
1322 **118**, 152503 (2017).
- 1323 [97] A. Tichai, E. Gebrerufael, K. Vobig, and R. Roth, Open-shell nuclei from no-core shell model
1324 with perturbative improvement, Phys. Lett. B **786**, 448 (2018).

1325

FIGURES

1326

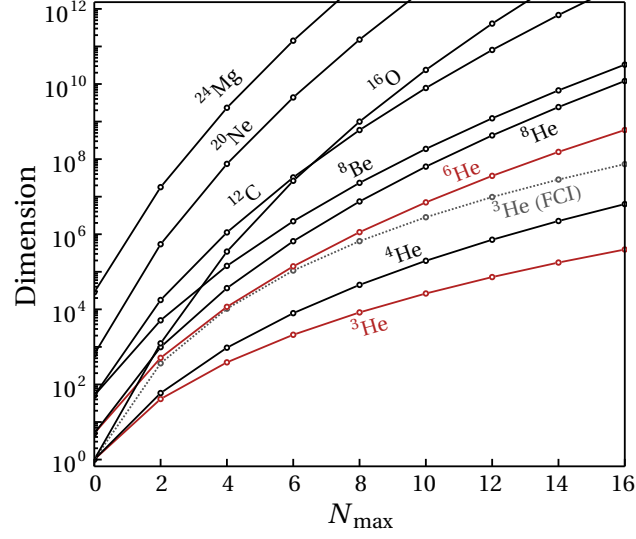


FIG. 1. Dimension of the NCCI many-body space as a function of the number of oscillator excitations N_{\max} included in the basis, including for $^3,^6\text{He}$ (highlighted). The dimension of the FCI space constructed from the same orbitals is also shown for ^3He (dotted gray line). Dimensions are those obtained with M -scheme bases ($M = 0$ for even-mass nuclei, or $M = 1/2$ for odd-mass nuclei) for the normal-parity space.

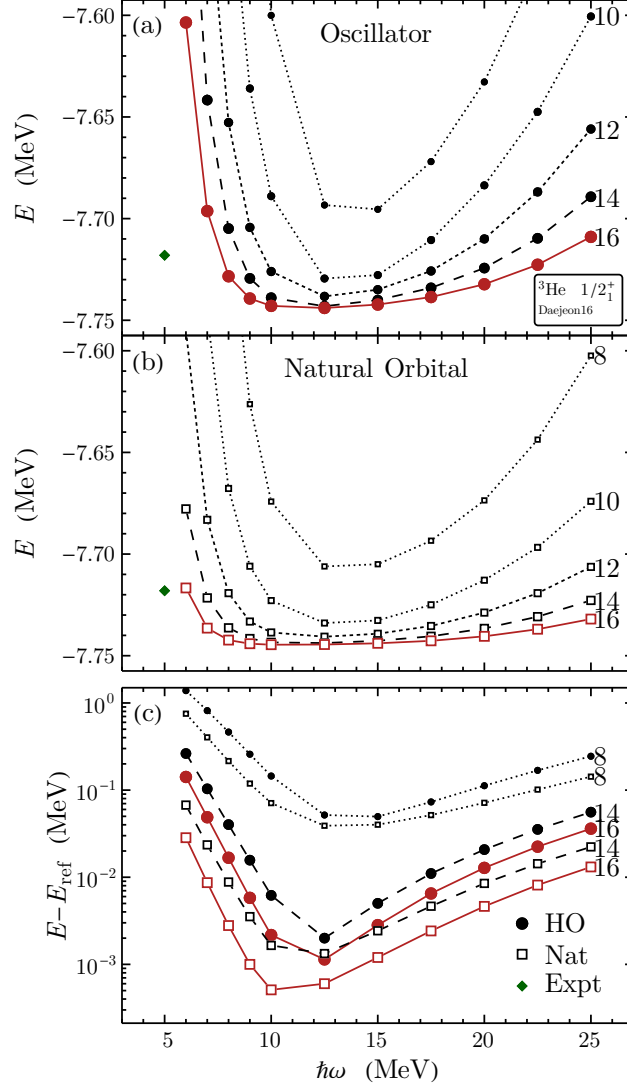


FIG. 2. Convergence of ^3He ground-state energy, as calculated in (a) oscillator (solid circles) and (b) natural-orbital (open squares) bases, shown also (c) on a logarithmic scale as the residual $E - E_{\text{ref}}$ with respect to the true “full-space” value. Calculated values are shown as functions of the basis parameter $\hbar\omega$, for successive even value of N_{max} , from $N_{\text{max}} = 8$ (dotted lines) to 16 (solid lines, highlighted). The experimental binding energy (solid diamond) [80] is also shown.

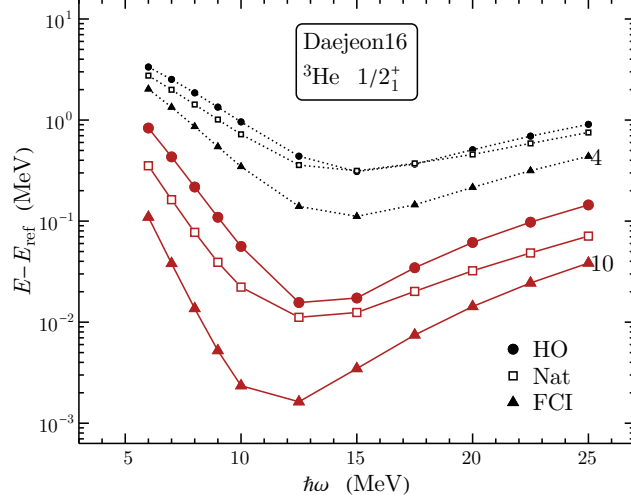


FIG. 3. Comparison of ${}^3\text{He}$ ground-state energies as calculated in spaces defined by N_{max} -truncated bases — oscillator (solid circles) or natural-orbital (open squares) — and the corresponding enveloping FCI space (solid triangles). Energies are shown as residuals, as in Fig. 2. Calculated values are shown as functions of the basis parameter $\hbar\omega$, for $N_{\text{max}} = 4$ (dotted lines) and 10 (solid lines, highlighted).

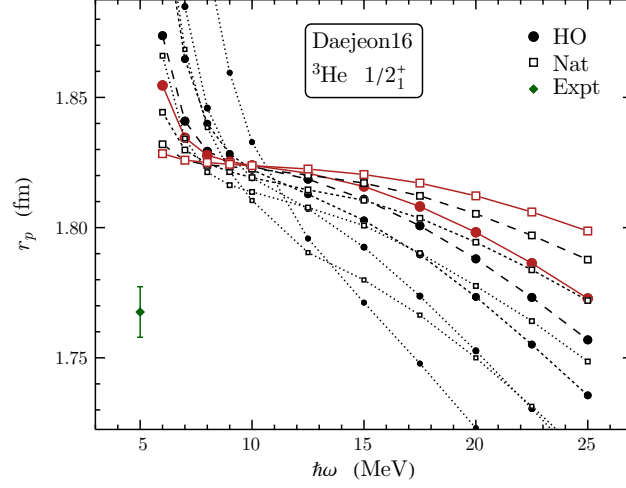


FIG. 4. Convergence of ^3He ground-state point-proton r.m.s. radius, as calculated in oscillator (solid circles) and natural-orbital (open squares) bases. Calculated values are shown as functions of the basis parameter $\hbar\omega$, for successive even value of N_{max} , from $N_{\text{max}} = 8$ (dotted lines) to 16 (solid lines, highlighted). The value deduced from the experimental charge radius [83] is also shown (filled diamond).

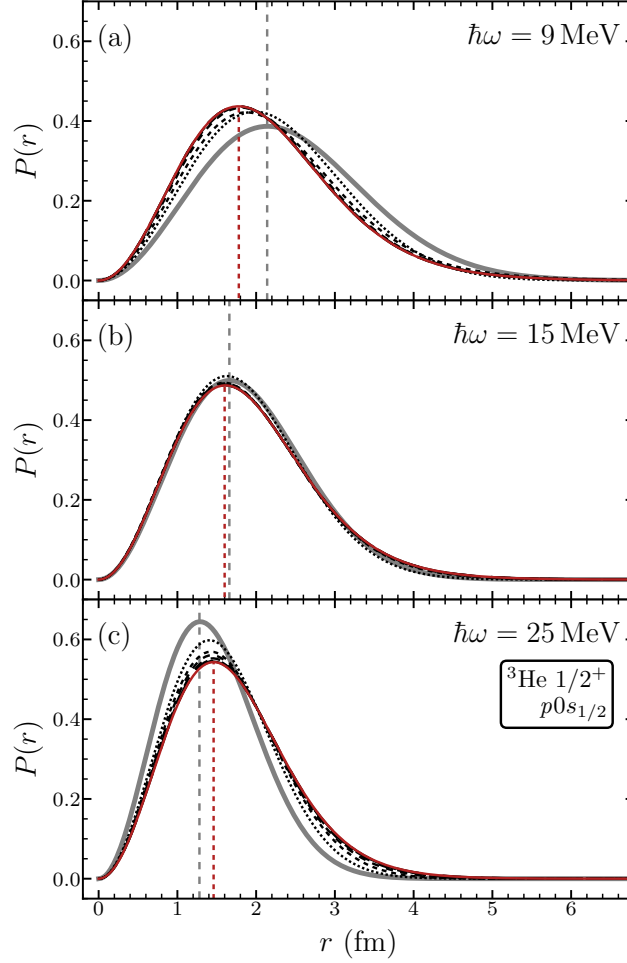


FIG. 5. Radial wave functions obtained for the ${}^3\text{He}$ proton $0s_{1/2}$ natural orbital, from different underlying oscillator-basis calculations, plotted as the radial probability density $P(r) = r^2|\psi(r)|^2$. Results are shown as obtained from underlying oscillator-basis calculations with (a) $\hbar\omega = 9$ MeV, (b) $\hbar\omega = 15$ MeV, and (c) $\hbar\omega = 25$ MeV. Radial wave functions are shown for $N_{\text{max}} = 2$ (dotted lines) through $N_{\text{max}} = 16$ (solid lines, highlighted), with the oscillator $0s$ function for the given $\hbar\omega$ (thick gray lines) shown for comparison. The locations of the peaks of the underlying harmonic-oscillator orbital and $N_{\text{max}} = 16$ natural orbital are marked with dashed vertical lines.

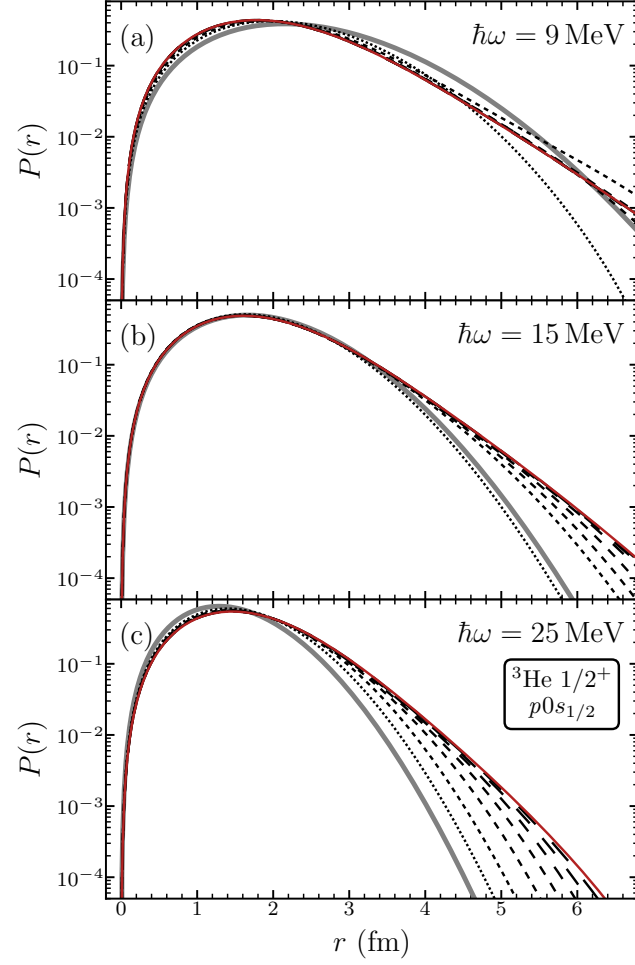


FIG. 6. Radial wave functions obtained for the ${}^3\text{He}$ proton $0s_{1/2}$ natural orbital, from different underlying oscillator-basis calculations, plotted as the radial probability density $P(r)$, as in Fig. 5, but now on a logarithmic scale.

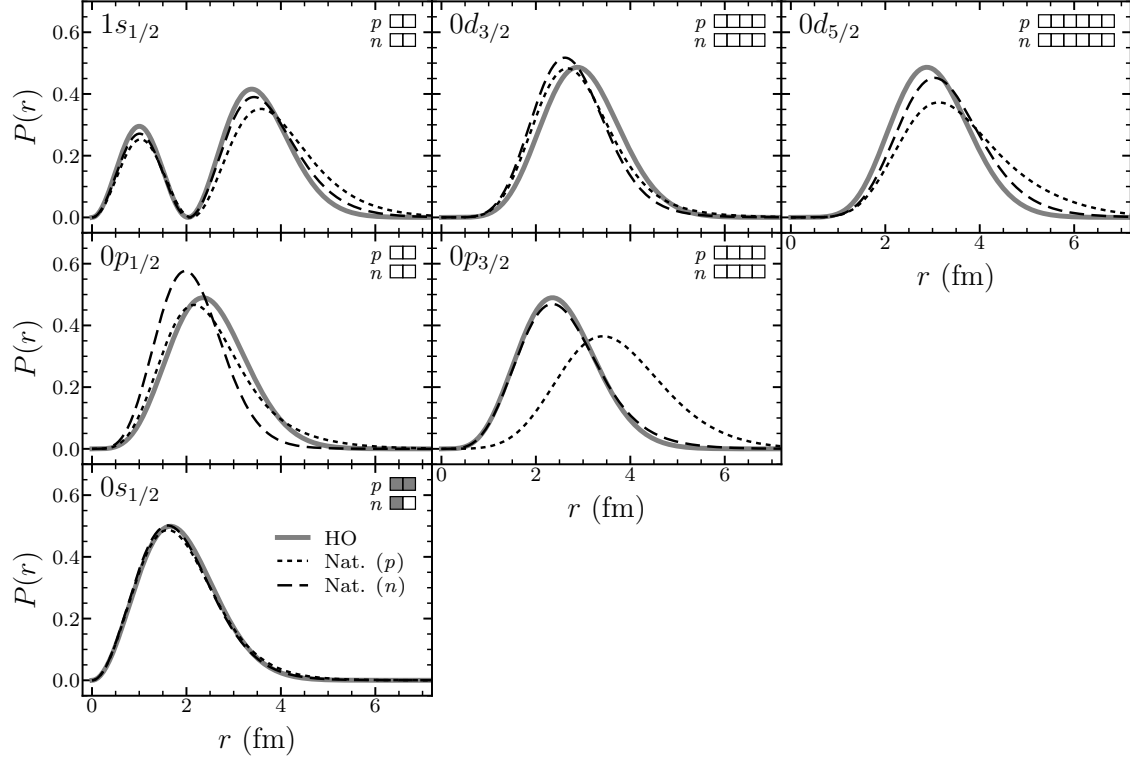


FIG. 7. Radial wave functions for the ${}^3\text{He}$ s -, p -, and sd -shell natural orbitals, for both protons (short dashed lines) and neutrons (long dashed lines), plotted as the radial probability density $P(r)$. These are obtained from the underlying oscillator-basis calculation near the variational minimum ($\hbar\omega = 15$ MeV) and at high N_{max} ($N_{\text{max}} = 16$). The corresponding oscillator radial functions for $\hbar\omega = 15$ MeV (thick gray lines) are shown for comparison. The mean occupancy n_a for each natural orbital, from the corresponding eigenvalue of the scalar density matrix, is indicated by the filling of the bar at top right (upper bar for protons, lower bar for neutrons).

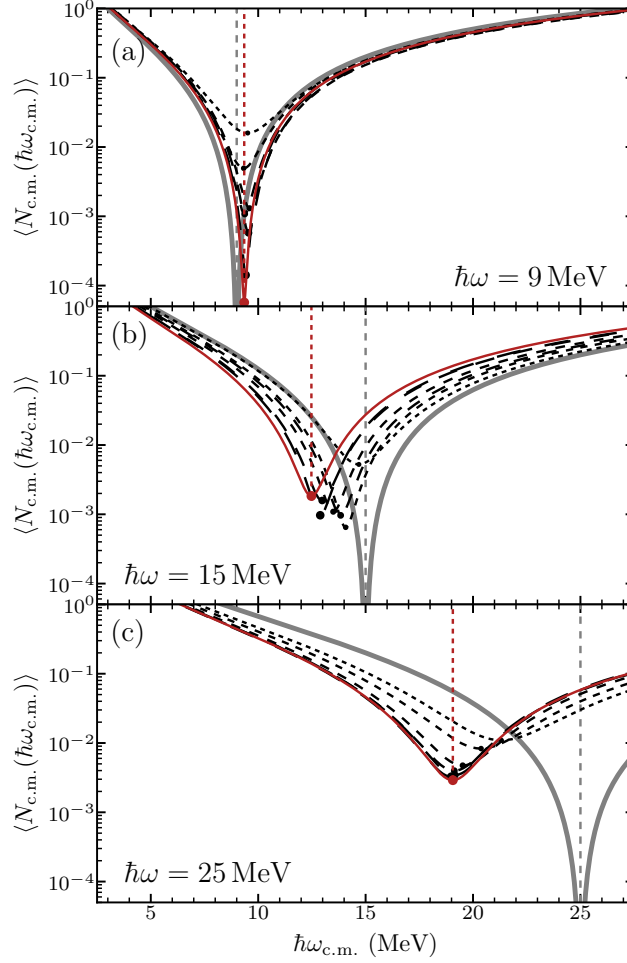


FIG. 8. Dependence of $\langle N_{c.m.} \rangle$ on $\hbar\omega_{c.m.}$, for ^3He ground state wave functions obtained in calculations with a natural-orbital basis, derived from underlying oscillator-basis calculations with (a) $\hbar\omega = 9 \text{ MeV}$, (b) $\hbar\omega = 15 \text{ MeV}$, and (c) $\hbar\omega = 25 \text{ MeV}$. Results are shown for calculations with $N_{\text{max}} = 4$ (short-dashed lines) through $N_{\text{max}} = 16$ (solid lines, highlighted), with the curve obtained for an oscillator $0s$ wave function with $\hbar\omega_{c.m.} = \hbar\omega$ (thick gray lines) — or, equivalently, the calculation in an $N_{\text{max}} = 0$ natural-orbital basis — shown for comparison. The underlying oscillator basis $\hbar\omega$ is indicated (dotted vertical line), as are the minimal $\hbar\tilde{\omega}_{c.m.}$ and $\tilde{N}_{c.m.}$ for each curve (dots, with dotted vertical line at highest N_{max}).

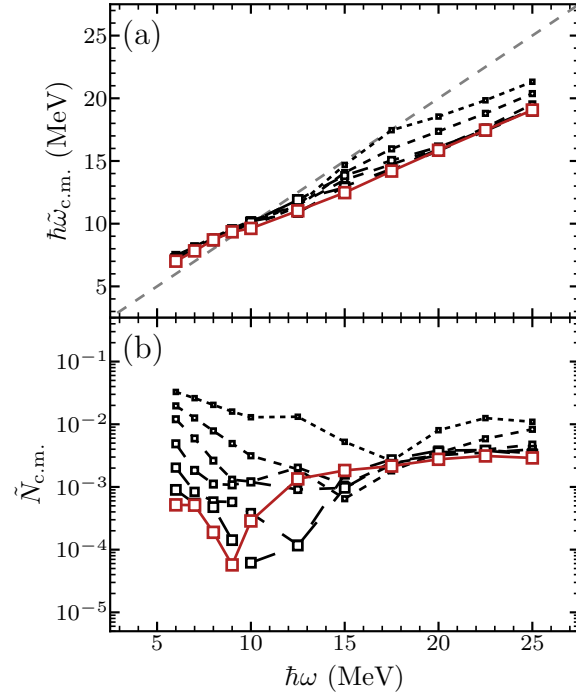


FIG. 9. Dependence of the approximate $0s$ center-of-mass motion of the calculated ${}^3\text{He}$ ground state (and its degree of contamination) on the $\hbar\omega$ of the underlying oscillator basis, in calculations with a natural-orbital basis, as measured by (a) $\hbar\tilde{\omega}_{\text{c.m.}}$ and (b) $\tilde{N}_{\text{c.m.}}$. Results are shown for calculations with $N_{\text{max}} = 4$ (dotted lines) through $N_{\text{max}} = 16$ (solid lines, highlighted).

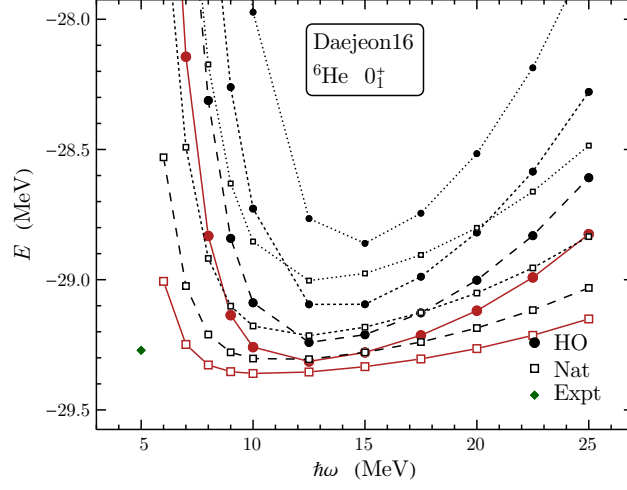


FIG. 10. The ${}^6\text{He}$ ground-state energy, as calculated in oscillator (solid circles) and natural orbital (open squares) bases. Calculated values are shown as functions of the basis parameter $\hbar\omega$, for successive even value of N_{max} , from $N_{\text{max}} = 8$ (dotted lines) to 14 (solid lines, highlighted). The experimental binding energy [80] is also shown (filled diamond).

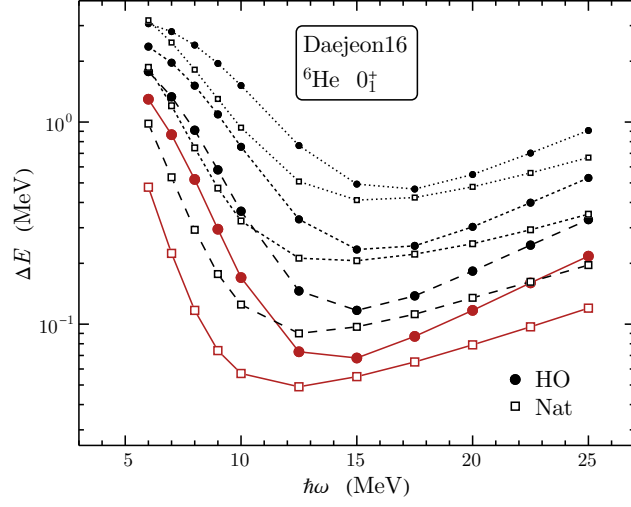


FIG. 11. Differences of calculated ${}^6\text{He}$ ground-state energies obtained for successive N_{max} , as obtained for oscillator (solid circles) and natural orbital (open squares) bases, shown on a logarithmic scale.

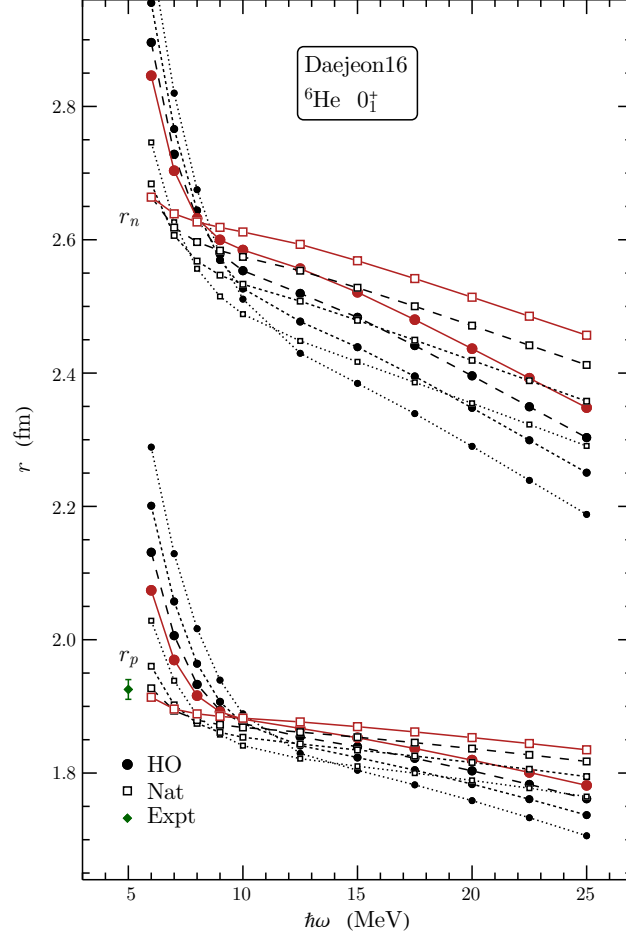


FIG. 12. The ${}^6\text{He}$ ground-state point-proton and point-neutron r.m.s. radii, as calculated in oscillator (solid circles) and natural orbital (open squares) bases. Calculated values are shown as functions of the basis parameter $\hbar\omega$, for successive even value of N_{max} , from $N_{\text{max}} = 8$ (dotted lines) to 14 (solid lines, highlighted). The value deduced from the experimental charge radius [83] is also shown (filled diamond).

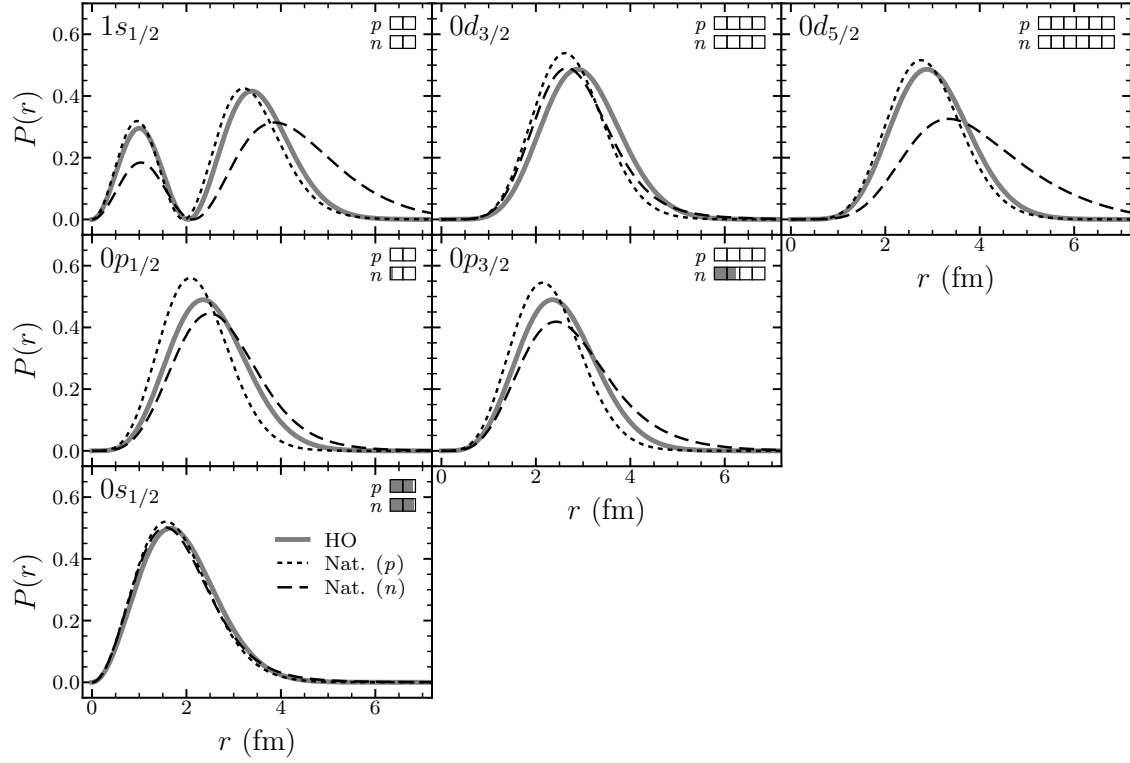


FIG. 13. Radial wave functions for the ${}^6\text{He}$ s -, p -, and sd -shell natural orbitals, for both protons (short dashed lines) and neutrons (long dashed lines), plotted as the radial probability density $P(r)$. These are obtained from the underlying oscillator-basis calculation near the variational minimum ($\hbar\omega = 15$ MeV) and at high N_{max} ($N_{\text{max}} = 14$). The corresponding oscillator radial functions for $\hbar\omega = 15$ MeV (thick gray lines) are shown for comparison. The mean occupancy n_a for each natural orbital, from the corresponding eigenvalue of the scalar density matrix, is indicated by the filling of the bar at top right (upper bar for protons, lower bar for neutrons).

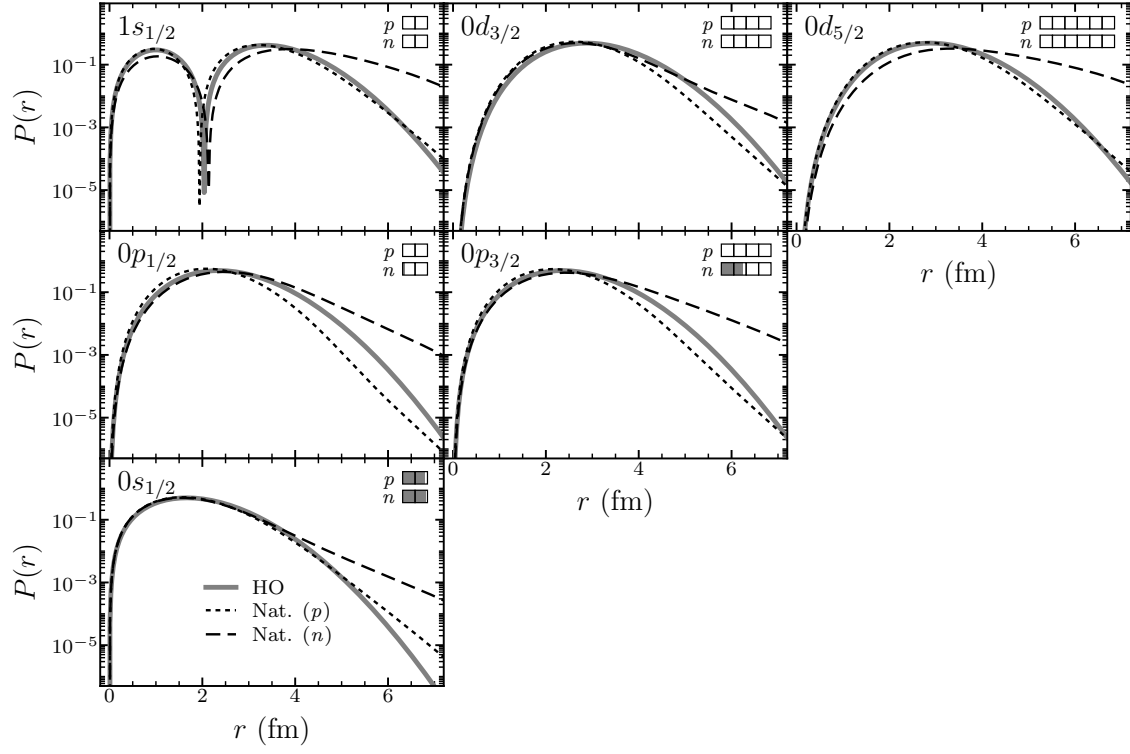


FIG. 14. Radial wave functions for the ${}^6\text{He}$ s -, p -, and sd -shell natural orbitals, plotted as the radial probability density $P(r)$, as in Fig. 13, but now on a logarithmic scale.

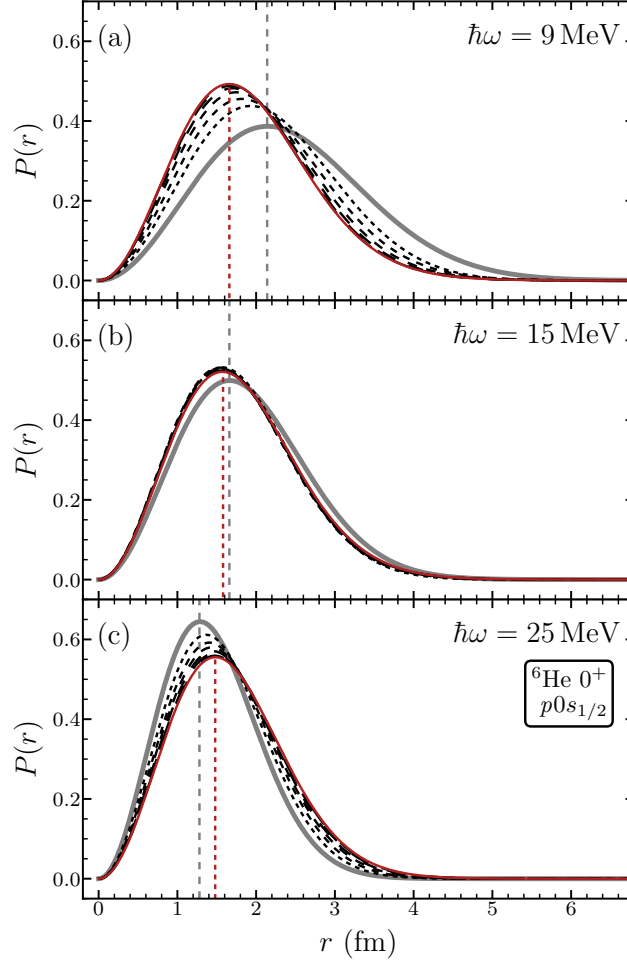


FIG. 15. Radial wave functions obtained for the ${}^6\text{He}$ proton $0s_{1/2}$ natural orbital, from different underlying oscillator-basis calculations, plotted as the radial probability density $P(r)$. Results are shown as obtained from underlying oscillator-basis calculations with (a) $\hbar\omega = 9\text{ MeV}$, (b) $\hbar\omega = 15\text{ MeV}$, and (c) $\hbar\omega = 25\text{ MeV}$. Radial wave functions are shown for $N_{\text{max}} = 2$ (dotted lines) through $N_{\text{max}} = 14$ (solid lines, highlighted), with the oscillator $0s$ function for the given $\hbar\omega$ (thick gray lines) shown for comparison. The locations of the peaks of the underlying harmonic-oscillator orbital and $N_{\text{max}} = 14$ natural orbital are marked with dashed vertical lines.

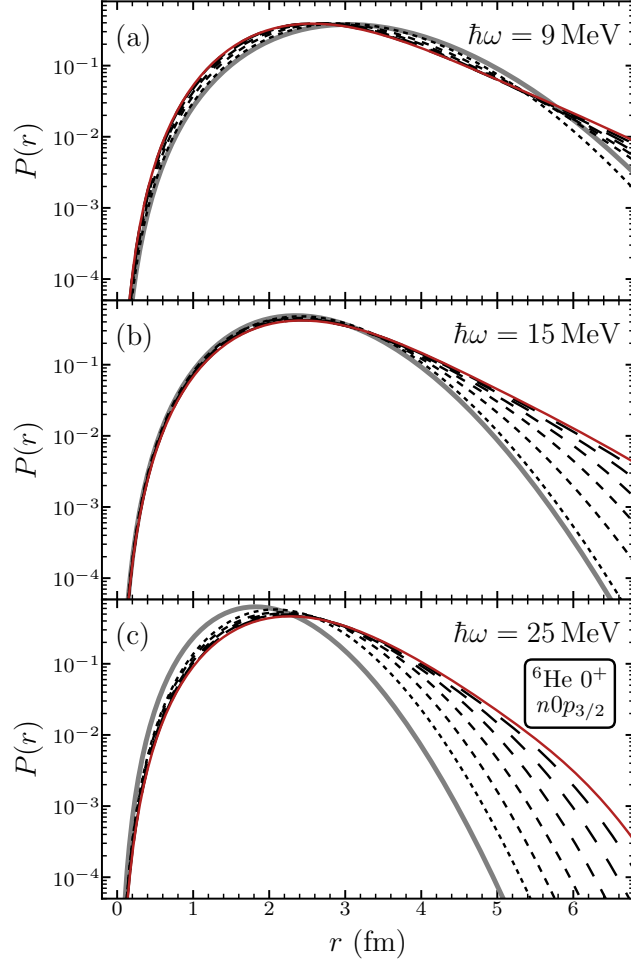


FIG. 16. Radial wave functions obtained for the ${}^6\text{He}$ neutron $0p_{3/2}$ natural orbital, from different underlying oscillator-basis calculations, plotted as the radial probability density $P(r)$, on a logarithmic scale. Results are shown as obtained from underlying oscillator-basis calculations with (a) $\hbar\omega = 9\text{ MeV}$, (b) $\hbar\omega = 15\text{ MeV}$, and (c) $\hbar\omega = 25\text{ MeV}$. Radial wave functions are shown for $N_{\text{max}} = 2$ (dotted lines) through $N_{\text{max}} = 14$ (solid lines, highlighted), with the oscillator $0s$ function for the given $\hbar\omega$ (thick gray lines) shown for comparison.

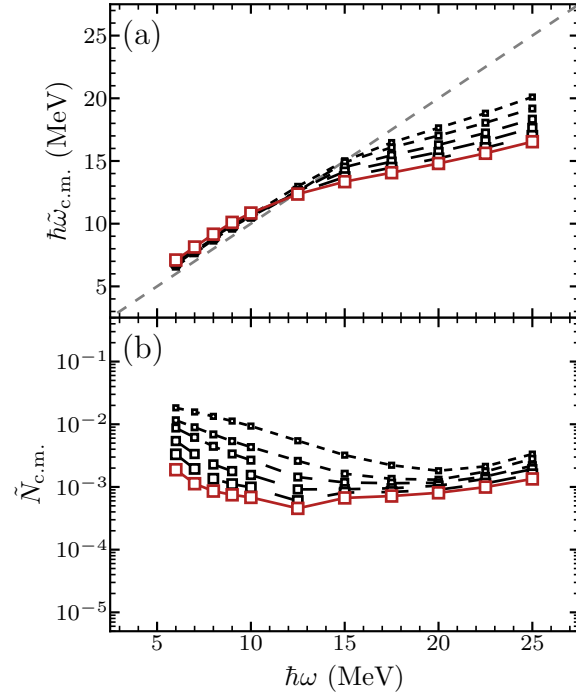


FIG. 17. Dependence of the approximate $0s$ center-of-mass motion of the calculated ${}^6\text{He}$ ground state (and its degree of contamination) on the $\hbar\omega$ of the underlying oscillator basis, in calculations with a natural-orbital basis, as measured by (a) $\hbar\tilde{\omega}_{\text{c.m.}}$ and (b) $\tilde{N}_{\text{c.m.}}$. Results are shown for calculations with $N_{\text{max}} = 4$ (dotted lines) through $N_{\text{max}} = 14$ (solid lines, highlighted).